



HAL
open science

**Stellar mass spectrum within massive collapsing clumps.
II. Thermodynamics and tidal forces of the first Larson
core. A robust mechanism for the peak of the IMF**

Yueh-Ning Lee, Patrick Hennebelle

► **To cite this version:**

Yueh-Ning Lee, Patrick Hennebelle. Stellar mass spectrum within massive collapsing clumps. II. Thermodynamics and tidal forces of the first Larson core. A robust mechanism for the peak of the IMF: II. Thermodynamics and tidal forces of the first Larson core. A robust mechanism for the peak of the IMF. *Astronomy and Astrophysics - A&A*, 2018, 611, pp.A89. 10.1051/0004-6361/201731523 . hal-02303494

HAL Id: hal-02303494

<https://hal.science/hal-02303494>

Submitted on 26 Apr 2023

HAL is a multi-disciplinary open access archive for the deposit and dissemination of scientific research documents, whether they are published or not. The documents may come from teaching and research institutions in France or abroad, or from public or private research centers.

L'archive ouverte pluridisciplinaire **HAL**, est destinée au dépôt et à la diffusion de documents scientifiques de niveau recherche, publiés ou non, émanant des établissements d'enseignement et de recherche français ou étrangers, des laboratoires publics ou privés.

Stellar mass spectrum within massive collapsing clumps

II. Thermodynamics and tidal forces of the first Larson core. A robust mechanism for the peak of the IMF

Yueh-Ning Lee (李悅寧)^{1,2,3} and Patrick Hennebelle^{1,2,4}

¹ IRFU, CEA, Université Paris-Saclay, 91191 Gif-sur-Yvette, France
e-mail: yueh-ning.lee@cea.fr

² Université Paris Diderot, AIM, Sorbonne Paris Cité, CEA, CNRS, 91191 Gif-sur-Yvette, France

³ Institut de Physique du Globe de Paris, Sorbonne Paris Cité, Université Paris Diderot, UMR 7154 CNRS, 75005 Paris, France

⁴ LERMA (UMR CNRS 8112), Ecole Normale Supérieure, 75231 Paris Cedex, France

Received 6 July 2017 / Accepted 4 November 2017

ABSTRACT

Context. Understanding the origin of the initial mass function (IMF) of stars is a major problem for the star formation process and beyond.

Aims. We investigate the dependence of the peak of the IMF on the physics of the so-called first Larson core, which corresponds to the point where the dust becomes opaque to its own radiation.

Methods. We performed numerical simulations of collapsing clouds of $1000 M_{\odot}$ for various gas equations of state (eos), paying great attention to the numerical resolution and convergence. The initial conditions of these numerical experiments are varied in the companion paper. We also develop analytical models that we compare to our numerical results.

Results. When an isothermal eos is used, we show that the peak of the IMF shifts to lower masses with improved numerical resolution. When an adiabatic eos is employed, numerical convergence is obtained. The peak position varies with the eos, and using an analytical model to infer the mass of the first Larson core, we find that the peak position is about ten times its value. By analyzing the stability of nonlinear density fluctuations in the vicinity of a point mass and then summing over a reasonable density distribution, we find that tidal forces exert a strong stabilizing effect and likely lead to a preferential mass several times higher than that of the first Larson core.

Conclusions. We propose that in a sufficiently massive and cold cloud, the peak of the IMF is determined by the thermodynamics of the high-density adiabatic gas as well as the stabilizing influence of tidal forces. The resulting characteristic mass is about ten times the mass of the first Larson core, which altogether leads to a few tenths of solar masses. Since these processes are not related to the large-scale physical conditions and to the environment, our results suggest a possible explanation for the apparent universality of the peak of the IMF.

Key words. ISM: clouds – ISM: structure – turbulence – stars: formation

1. Introduction

Star formation is believed to have major consequences on the structure of our Universe. In spite of sustained efforts, the origin of the initial mass function (IMF) in particular is still a matter of debate (e.g., [Offner et al. 2014](#)). While the gravo-turbulent fragmentation of cold dense molecular gas is a widely accepted scenario of star formation, it is in apparent contradiction with the observed IMF exhibiting no significant variation among different environments (e.g., [Kroupa 2001](#); [Chabrier 2003](#); [Bastian et al. 2010](#); [Offner et al. 2014](#)), although [Dib et al. \(2017\)](#) found more variations than are commonly assumed.

In particular, the physical origin of the peak of the IMF, around $0.3 M_{\odot}$, is still uncertain. Several ideas have been proposed, which fall into three categories that are not mutually exclusive. First, it has been proposed that the thermodynamics of the gas could provide a particular density to which a Jeans mass is associated. For example, [Larson \(1985\)](#) computed the gas temperature in dense core conditions and concluded that owing to molecular cooling, the effective adiabatic exponent, γ_{ad} , is expected to be on the order of 0.7 for densities below $\approx 10^5 \text{ cm}^{-3}$, while at higher densities, $\gamma_{\text{ad}} \approx 1$ as a result of gas-dust coupling.

Since the fragmentation sensitively depends on γ_{ad} , the question arises as to whether the change of the effective equation of state at $\approx 10^5 \text{ cm}^{-3}$ could lead to a particular Jeans mass, which for a temperature of 10 K is $\sim 0.3 M_{\odot}$. A similar, though not identical, line of explanations has been put forward by [Elmegreen et al. \(2008\)](#): the thermodynamics of the gas in various environments could result in a Jeans mass that weakly depends on the gas density. The second category of explanations has been proposed by [Bate \(2009b\)](#), [Krumholz \(2011\)](#), and [Guszejnov et al. \(2016\)](#). The idea is that because of the heating from the accretion luminosity, the gas temperature increases in the vicinity of the protostar, and therefore the local increase of the Jeans mass leads to a possible self-regulation. Again, these studies infer that the Jeans mass has a weaker dependence on the gas density than in an isothermal gas. Finally, the third category of explanations invokes a compensation between the density and the velocity dispersion, which vary in opposite directions with clump masses through Larson relations ([Hennebelle 2012](#); [Lee & Hennebelle 2016b](#)). Considering clumps of increasingly higher mass, the density decreases with the mass, which in turn increases the Jeans mass, while the increasing Mach number tends to create denser gas through shocks, yielding a slowly varying characteristic mass. None of

these explanations is well established yet. For example, while it has been suggested by various simulations (e.g., Jappsen et al. 2005; Bate 2009b) that thermodynamics influences the mass spectrum of the objects that form, there is no well-established set of simulations demonstrating the invariance of the peak of the IMF for a broad range of physical conditions.

In the companion paper (Lee & Hennebelle 2018, hereafter Paper I), we conduct a systematic exploration of the initial conditions by varying the initial density and turbulence of the molecular cloud. The physics is greatly simplified at this stage because our goal is to identify the physical processes at play. At relatively high densities ($\geq 10^5 \text{ cm}^{-3}$), the shape of the stellar distribution, including the peak position and the high-mass end slope, becomes no longer dependent on the global density of the parent molecular cloud. This means that some physical mechanisms are operating at local scales and do not depend on the large ones, such as the collapsing clump itself. This result is surprising at first because the mean Jeans mass changes by more than one order of magnitude in our series of simulations. Moreover, the thermodynamics treated in these simulations assumes that the gas remains isothermal up to a density of a few 10^{10} cm^{-3} , where the gas becomes adiabatic. While in the context of a collapsing clump, the isothermal regime does not provide any characteristic mass, the adiabatic regime does, because the Jeans mass increases with increasing density. The lowest Jeans mass, estimated at the density where the gas becomes adiabatic, is a few $10^{-3} M_{\odot}$ (Rees 1976; Whitworth et al. 2007) and therefore is almost two orders of magnitude lower than the peak position of the stellar distribution around $0.1 M_{\odot}$ observed in the simulations. Consequently, the origin of a characteristic mass in our simulations is not obvious and needs to be elucidated. For this purpose, we perform in this paper a series of simulations with initial conditions identical to those in Paper I, while altering the gas equation of state (eos). With the variation of the stellar distribution peak position (around $0.1 M_{\odot}$) with respect to the varying eos, we try to shed light on the mechanisms that determine the IMF peak mass.

In the second section, we present the numerical setup we employed, including the initial conditions and the various eos used throughout the paper. In the third section, we present the results of the numerical simulations. In the fourth section, we infer the mass of the first Larson cores for various eos, and we study its correlation with the mass spectrum peak in the simulations. In the fifth section, we develop an analytical model that accounts for the factor, on the order of ten, between the mass of the first Larson core and the peak of the stellar distribution obtained from numerical simulations. In the sixth section, we provide a discussion of our results. The seventh section concludes the paper.

2. Numerical setup and initial conditions

2.1. Numerical setup and runs

We used the adaptive mesh refinement (AMR) magnetohydrodynamics code RAMSES (Teyssier 2002; Fromang et al. 2006) to evolve the hydrodynamical equations. Simulations were initialized with a Bonner-Ebert-like spherical molecular cloud with a density profile $\rho(r) = \rho_0 / [1 + (r/r_0)^2]$, where r_0 is the size of central plateau and r the distance to the cloud center, as described in Paper I (see more details therein).

Run C1 in Paper I is used as the canonical run here and is labeled C10h, as we present below. The cloud has $1000 M_{\odot}$

and 0.084 pc radius, with the simulation box twice the size of the cloud. The central density $n_0 = \rho_0 / (\mu m_p) \simeq 6 \times 10^7 \text{ cm}^{-3}$, where $\mu = 2.33$ is the mean molecular weight and m_p is the atomic hydrogen mass. We note that this density is very high and may not be realistic to describe most Milky Way clouds. However, our goal here is to investigate the physical processes rather than performing a detailed comparison with observations. A turbulent velocity field following a Kolmogorov spectrum with random phases was seeded, and a relaxation phase without self-gravity was run during $\sim 30\%$ of the turbulence-crossing time on the base grid (2^8) to prepare for coherent density and velocity fluctuations. Initially, the turbulence was a mix of compressive and solenoidal modes with an energy ratio 1:2. The AMR scheme requires that the local Jeans length is always resolved by ten cells. The canonical run had a maximum refinement of 14 levels, corresponding to 4 AU resolution, while higher and lower resolution runs were also performed. The simulation parameters are listed in Table 1.

2.2. Equation of state

In a dense core, the temperature is about 10 K, except at high density, where the gas is optically opaque to its own radiation and is nearly adiabatic (e.g., Masunaga et al. 1998; Vaytet et al. 2012; Vaytet & Haugbølle 2017). The temperature T , which depends on the gas density ρ , is described with the eos

$$T = T_0 \left[1 + (\rho/\rho_{\text{ad}})^{(\gamma-1)} \right], \quad (1)$$

where the isothermal temperature T_0 at low density is set to 10 K. We studied the effect of the eos by varying the critical turnover density ρ_{ad} , which designates the change between isothermal behavior and adiabatic heating, and the polytropic index γ , which describes the heating rate. The polytropic index of molecular hydrogen is $\gamma_1 = 5/3$ and $\gamma_2 = 7/5$ before and after the excitation of rotation modes of hydrogen molecules at around 100 K. At $\sim 1000 \text{ K}$, the H_2 molecules start to dissociate and γ drops to $\gamma_3 \sim 1.1$. In this study, we aim to examine the effect of thermodynamics on the final mass a star can reach. We therefore also considered a more complete description of a full eos,

$$T = T_0 \left\{ 1 + \frac{(\rho/\rho_{\text{ad}})^{(\gamma_1-1)}}{[1 + (\rho/\rho_{\text{ad},2})^{(\gamma_1-\gamma_2)n} (1 + (\rho/\rho_{\text{ad},3})^{(\gamma_2-\gamma_3)n})]^{1/n}} \right\}, \quad (2)$$

where $n = 3$ is a smoothing parameter. This barotropic eos is employed for convenience. It signifies effectively $T \propto \rho^{\gamma-1}$ with $\gamma = 1$ for $\rho < \rho_{\text{ad}}$, $\gamma = \gamma_1$ for $\rho_{\text{ad}} < \rho < \rho_{\text{ad},2}$, $\gamma = \gamma_2$ for $\rho_{\text{ad},2} < \rho < \rho_{\text{ad},3}$, and $\gamma = \gamma_3$ for $\rho > \rho_{\text{ad},3}$. In the following studies, we fixed $\rho_{\text{ad},2} = 30 \rho_{\text{ad}}$ and $\rho_{\text{ad},3} = 1000 \rho_{\text{ad},2}$.

As shown in Table 1, $n_{\text{ad}} = \rho_{\text{ad}} / (\mu m_p)$ is varied between 10^9 cm^{-3} and 10^{10} cm^{-3} , while using a hard eos $\gamma = 5/3$ or a soft one $\gamma = 4/3$. We also study the effects of a full eos that describes the transition of γ from 1 to $5/3$, $7/5$, and then 1.1. The two latter transitions correspond roughly to $T = 100$ and 1000 K . We also set $n_{\text{ad}} = 10^{13} \text{ cm}^{-3}$ in run I, that is practically isothermal since such high density is hardly reached at this resolution.

2.3. Sink particle algorithm

We used the sink particle algorithm from Bleuler & Teyssier (2014) (see also Krumholz et al. 2004; Federrath et al. 2010), and we briefly describe it here. Sink particles are formed at the highest refinement level. The algorithm first identifies local

Table 1. Simulation parameters.

Label	$n_{\text{ad}} (10^9 \text{ cm}^{-3})$	$n_{\text{sink}} (10^9 \text{ cm}^{-3})$	γ	l_{max}	Resolution (AU)
C10h	10	10	5/3	14	4
C10h+	10	10	5/3	15	2
C10h-	10	10	5/3	13	8
C10h--	10	10	5/3	12	17
C3h-	3	1	5/3	13	8
C1h	1	1	5/3	14	4
C1h-	1	1	5/3	13	8
C1h-*	1	1	5/3	13	8
C1h--	1	1	5/3	12	17
C1hd-o	1	100	5/3	13	8
C10s-	10	1	4/3	13	8
C1s-	1	1	4/3	13	8
C10f	10	10	5/3, 7/5, 1.1	14	4
C1f	1	10	5/3, 7/5, 1.1	14	4
C10fd	10	300	5/3, 7/5, 1.1	14	4
I	10^4	10	1	14	4
I-	10^4	1	1	13	8
I--	10^4	1	1	12	17

Notes: Columns are: the label, the density n_{ad} at which the eos switches from isothermal to adiabatic as defined in Eq. (1), the minimum density n_{sink} at which the sink is introduced, the polytropic index γ , the maximum refinement level l_{max} , and the physical resolution. The temperature remains 10 K at density below n_{ad} . When the full eos is used, the second and third adiabatic index switches occur at $30 n_{\text{ad}}$ and $30\,000 n_{\text{ad}}$, corresponding roughly to 100 K and 1000 K, respectively. In the labels, “C/T” stands for adiabatic/isothermal eos, the number is the value of n_{ad} , “h/s/f” stands for hard/soft/full eos, “+/-” is for higher/lower resolution, “d” stands for higher sink density threshold, the asterisk represents a stricter clump merging scheme, and “o” stands for density threshold criteria for sinks alone.

density concentrations, which are referred to as clumps, above a given density threshold (we typically used 1/10 of the density threshold for sink particles n_{sink}). Connected clumps are merged if the density contrast between the peak and the saddle point is less than two. The final clumps are then passed on for a sink formation check.

The clump peak undergoes several criteria before a sink formation site is flagged. First, a density threshold is imposed such that the peak must have a density higher than n_{sink} , which we varied between 10^{10} and 3×10^{11} to investigate its influence. Second, additional criteria are used to check whether the clump is virially bound and has a converging flow. A sink particle is placed at the density peak when all criteria are satisfied. Simple density thresholding was used in runs C1hd-o to study the numerical effects of the algorithm. The sink then interacts gravitationally with the gas component as well as other sinks and accretes from the surrounding with a threshold scheme. When the cells surrounding the sink particle exceeds n_{sink} , 75 percent (this numerical factor seems not to have a crucial effect on our results, see Appendix A) of the excessive gas mass in the cells is accreted onto the sink particle.

2.4. Missing physics

The physics was deliberately simplified because we tried to conduct a systematic set of simulations to clarify the influence of the initial conditions, eos, and resolution. Other processes not included here nonetheless play significant, possibly dominant roles. This is particularly the case for the accretion luminosity that emanates from the protostars (Krumholz et al. 2007b; Bate 2009b; Commerçon et al. 2011) and heats the gas, which in turn increases the thermal support. The magnetic field is

another important process (Hennebelle et al. 2011; Peters et al. 2011; Myers et al. 2013) that likely affects the fragmentation of clusters through magnetic braking and magnetic support; we do not consider this here.

3. Results: mass spectra in numerical simulations

3.1. Isothermal runs

The sink distributions displayed in Fig. 1 present a well-defined peak and a power law at high masses that is roughly $\propto M^{-1}$. The isothermal runs show that the stellar distribution peak moves from 0.05 to 0.01 M_{\odot} when we change the resolution from 17 to 4 AU. As the collapse of isothermal gas is self-similar, there is no characteristic scale or mass in such simulations at high density. Roughly speaking, when we double the resolution, the highest density that can be described increases by a factor of about $2^3 = 8$. We therefore may expect that the peak position shifts by $\approx \sqrt{64} = 8$ when two more refinement levels are introduced. This is compatible with the trend observed in Fig. 1.

The mass of sink particles therefore depends on the numerical resolution. This is likely what occurs in simulations that recovered the stellar distribution in a collapsing massive and isothermal cloud (e.g., Bonnell et al. 2006; Girichidis et al. 2011; Ballesteros-Paredes et al. 2015). Typically, the dependence of the peak position is expected once the collapsing cloud is sufficiently cold. It is worth emphasizing that this is not a statement about the absence of convergence of isothermal calculations in general. As shown in Girichidis et al. (2011) and in Paper I, initial conditions matter greatly. For example, Gong & Ostriker (2015) did obtain numerical convergence in their colliding flow calculations.

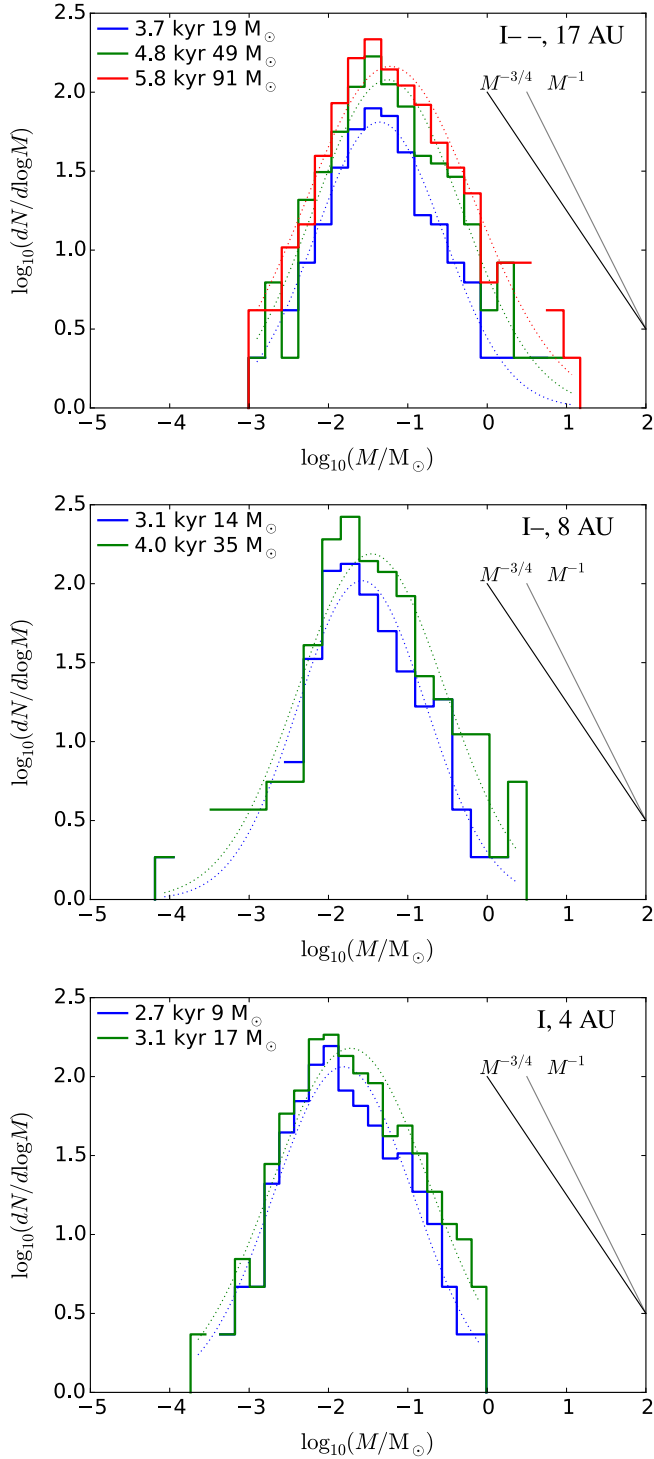


Fig. 1. Stellar distribution of isothermal runs with varied resolutions of 17, 8, and 4 AU in colored histograms, with time and total accreted mass shown in the legend. Lognormal fits are presented with dashed thin curves. Power laws of $M^{-3/4}$ and M^{-1} are shown for comparison with black and gray lines, respectively. The characteristic mass of the stellar distribution shifts to lower values with increasing resolution.

3.2. Runs with $\gamma = 5/3$

With $\gamma = 5/3$, the fiducial run (C10h) in Fig. 2 very quickly shows a well-defined stellar distribution that peaks at $\approx 0.1 M_{\odot}$. The runs with four resolutions, 2, 4, 8, and 17 AU, show that the peak position is robust and does not change significantly with the resolution. This is a noticeable difference to the isothermal

case. There is nevertheless some significant evolution of the mass spectra when the spatial resolution improves. First of all, the number of objects near the peak increases when the resolution improves from 17 to 4 AU (from $\log_{10}(dN/d\log M) \approx 1.6$ to ≈ 2.1 at the time when $200 M_{\odot}$ have been accreted), while this number does not seem to change significantly between the two highest resolutions (two bottom panels). As in the isothermal simulations, the high-mass part is also described by a power law $\propto M^{-1}$, although this is much clearer in the highest resolution runs.

Figure 3 reveals that n_{ad} has an effect on the peak position. With $n_{\text{ad}} = 10^9$, sinks are completely prevented from forming at the resolution of 4 AU (C1h, no mass spectra available). Decreasing the resolution allows sink particles to form. The run at 8 AU resolution (C1h-) produces top-heavy spectra with a loosely defined peak at $\approx 1 M_{\odot}$, while a coarser resolution at 17 AU (C1h-) shifts the peak to $\approx 0.3 M_{\odot}$ and more sinks are formed. This effect results from the excessive heating at high densities, where the approximated expression of one single γ value stops being physical, and the high-temperature gas is thus always thermally supported against collapse at the finest resolution scale and sink particles hardly form. This behavior is interpreted more quantitatively in Sect. 4. The run with $n_{\text{ad}} = 3 \times 10^9$ at 8 AU resolution (C3h-) produces mass spectra that peak at lower mass than that of run C1h- at same resolution.

These results suggest that the eos has a strong effect on the characteristic mass of the stellar distribution. Moreover, we find that the stellar distribution peak is significantly higher than the Jeans mass at which the gas becomes opaque to its radiation (typically on the order of $10^{-3} M_{\odot}$) or even the mass of the first Larson core (a few $10^{-2} M_{\odot}$). The link between the two is addressed in Sect. 4 and Sect. 5.

3.3. Runs with $\gamma = 4/3$

As revealed by Fig. 4 for runs using $\gamma = 4/3$, the peak shifts to slightly lower masses and the stellar distribution is slightly wider than with $\gamma = 5/3$. The run with $n_{\text{ad}} = 10^9 \text{ cm}^{-3}$ (C1s-) yields a slightly higher peak mass than that with $n_{\text{ad}} = 10^{10} \text{ cm}^{-3}$ (C10s-) since the heating starts at lower density, and thus the higher temperature at the same density provides more support against gravity. With $\gamma = 4/3$, the gas heats up less quickly as density increases than at $\gamma = 5/3$, and the high-density region suffers less from overheating (more sinks form in C1s- than C1h-).

3.4. Runs with a full eos

The first panel of Fig. 5 shows a very similar behavior to the fiducial run (C10h) and suggests that the $\gamma = 5/3$ part of the eos matters the most. To test the influence of the sink particle scheme, we have performed a run for which $n_{\text{sink}} = 3 \times 10^{11} \text{ cm}^{-3}$ (C10fd, second panel). Applying higher threshold for sinks does not affect the peak mass, while the low-mass end becomes less populated. This shows that the exact moment where the sink particles are introduced does not control the peak position, but has some influence on the distribution of low masses. This is compatible with the eos being the most important process that determines the peak position.

Finally, we also considered $n_{\text{ad}} = 10^9 \text{ cm}^{-3}$ using the full eos. The shift of the peak is as obvious with a full eos (C10f and C1f) as that with $\gamma = 5/3$. We note that in run C1f we overcome the overheating problem at high resolution that we encountered in run C1h. Gas is allowed to collapse and form sink particles

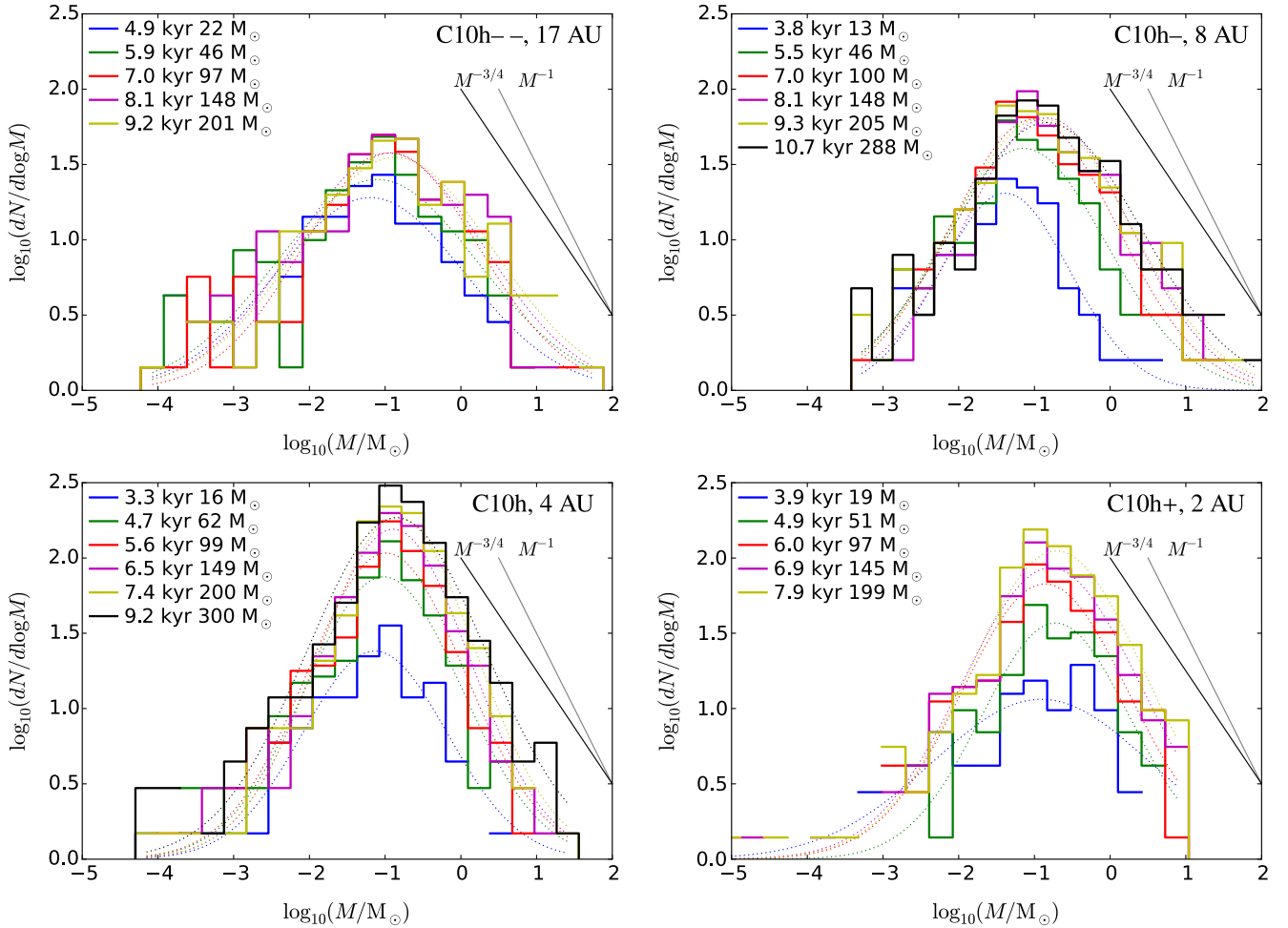


Fig. 2. Stellar distribution of runs with a smoothed two-slope polytropic eos with $\gamma = 5/3$ and $n_{\text{ad}} = 10^{10} \text{ cm}^{-3}$, with varying resolutions of 17, 8, 4, and 2 AU. The characteristic mass of the stellar distribution is $\approx 0.1 M_{\odot}$, regardless of numerical resolution.

without difficulty. This confirms that the determining part of the eos corresponds to $\gamma = 5/3$.

4. Mass of the first Larson core and peak of the sink distribution

As the previous section suggests that the thermodynamics is essential in determining the peak of the stellar distribution, we calculate the mass of the first Larson core and study its correlation with the peak mass obtained in the simulations.

4.1. First Larson core

As gravitational collapse proceeds, the density increases, and at some point, the dust becomes opaque to its own radiation. At this point, the gas becomes essentially adiabatic, and a so-called first Larson core forms (Larson 1969; Masunaga et al. 1998). While the gravitational energy can overcome the thermal support through contraction of an isothermal gas, gas with polytropic index $\gamma > 4/3$ can resist the collapse. The first Larson core grows in mass by accretion, leading to the increase of the central density and temperature. When the temperature reaches about 1500 K, molecular hydrogen starts dissociating and therefore efficiently cools the gas, and the gravitational collapse resumes, which eventually leads to the formation of the second Larson core, namely the protostar. To obtain a protostar,

it is probably necessary to accumulate sufficient mass to trigger the second collapse, and this process is essential in setting the peak of the stellar distribution. First Larson cores with lower masses cannot form protostars (or will do so through cooling, but on a longer timescale). While this process is not explicitly resolved in our simulations, the introduction of the sink particles to some extent mimics this sequence since they are introduced only when enough mass has been accumulated for the gas to be gravitationally unstable.

By integrating the hydrostatic equations of the gas, we deduce the density profile that a core develops before undergoing the secondary collapse. From the density profile, the mass can be inferred, provided that some radius can be estimated or specified. The equations of hydrostatic equilibrium are

$$\frac{dM}{dr} = 4\pi r^2 \rho, \quad (3)$$

$$\frac{1}{\rho} \frac{dP}{dr} = -\frac{GM}{r^2}, \quad (4)$$

where M , ρ , P , r , and G are the mass contained within a given radius, density, pressure, radius, and the gravitational constant. The derivative of Eq. (4) with respect to r yields

$$\frac{d}{dr} \left(\frac{1}{\rho} \frac{dP}{dr} \right) = \frac{2GM}{r^3} - \frac{G}{r^2} \frac{dM}{dr} = -\frac{2}{\rho r} \frac{dP}{dr} - 4\pi G \rho, \quad (5)$$

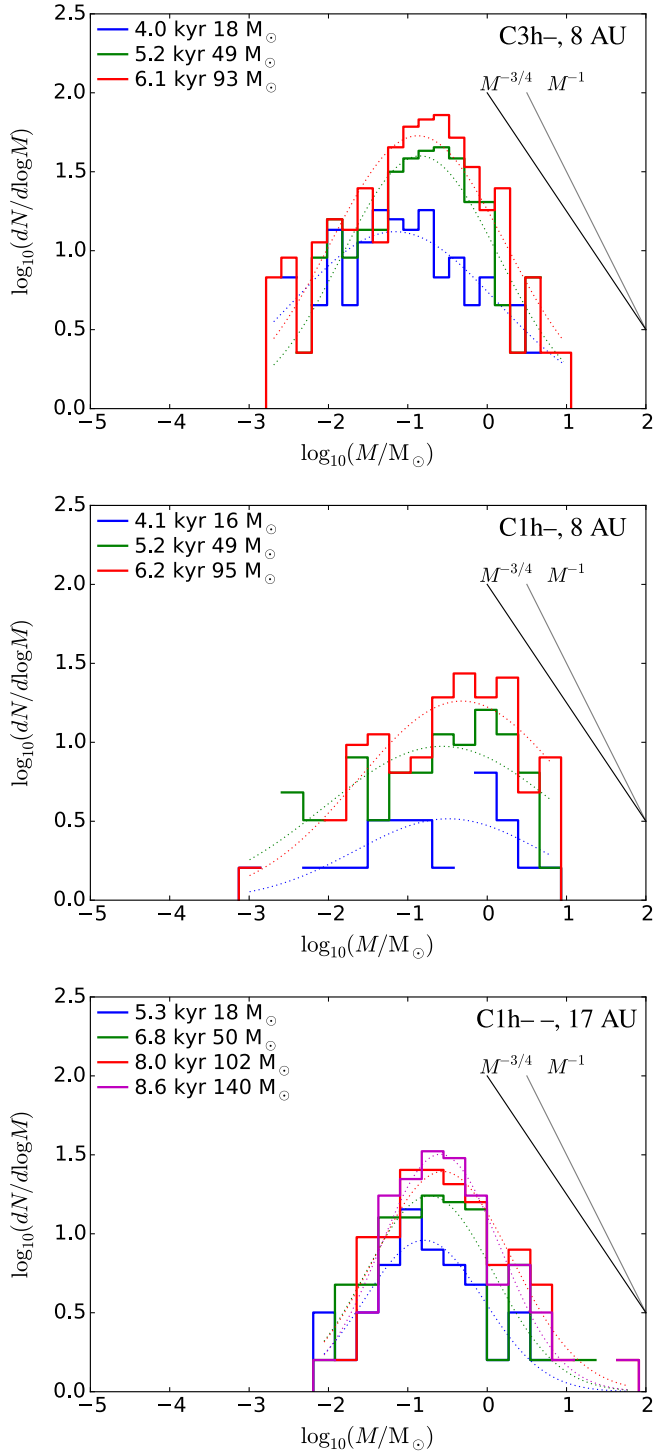


Fig. 3. Stellar distributions of runs with a smoothed two-slope polytropic eos with $\gamma = 5/3$, lowered n_{ad} at 3×10^9 (C3h-) and 10^9 cm^{-3} (C1h-, C1h--). The characteristic mass of the stellar distribution increases with decreasing n_{ad} . At $n_{\text{ad}} = 10^9 \text{ cm}^{-3}$, the stellar distribution becomes top-heavy with improved resolution from 17 to 8 AU.

where the second equality is obtained by substituting with Eqs. (3) and (4). The pressure is related to the density by the eos that we used in the simulations,

$$P = \frac{k_B \rho T(\rho)}{\mu m_p}, \quad (6)$$

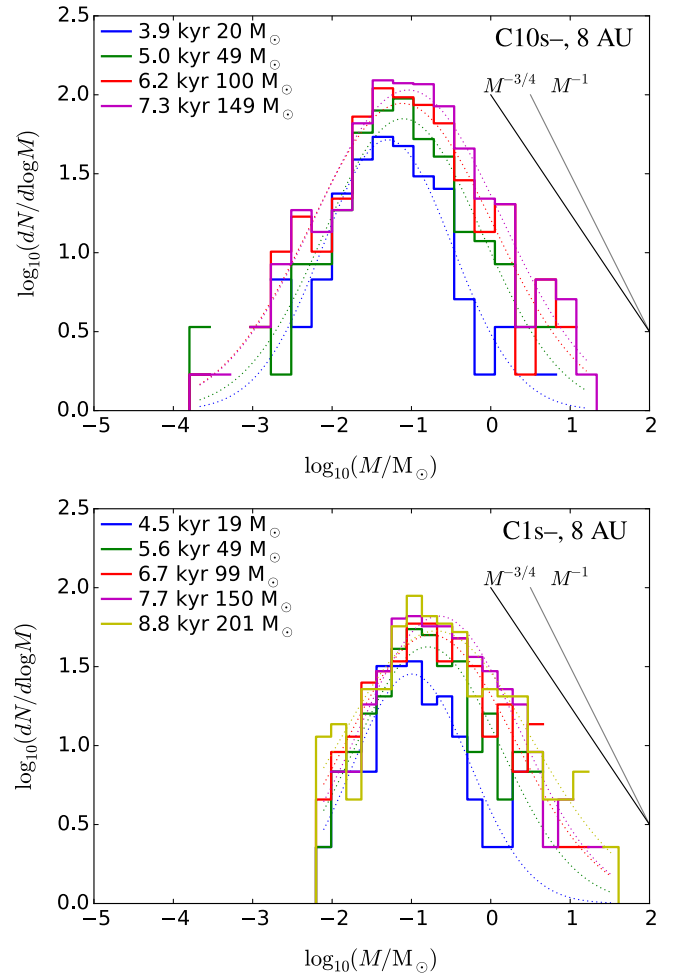


Fig. 4. Stellar distributions of runs with a smoothed two-slope polytropic eos with $\gamma = 4/3$, $n_{\text{ad}} = 10^{10} \text{ cm}^{-3}$ (C10s-) and 10^9 cm^{-3} (C1s-). The characteristic mass of the stellar distribution increases by a factor ~ 3 when n_{ad} is lowered by a factor ten.

where k_B is the Boltzmann constant, and the temperature $T(\rho)$ is given by Eqs. (1) or (2).

This results in a second-order differential equation of ρ that we can solve numerically using standard Runge-Kutta methods:

$$\left[\frac{dT}{d\rho} + \frac{T}{\rho} \right] \frac{d^2 \rho}{dr^2} = \left[\frac{T}{\rho^2} - \frac{1}{\rho} \frac{dT}{d\rho} - \frac{dT^2}{d^2 \rho} \right] \left(\frac{d\rho}{dr} \right)^2 + \frac{2GM\mu m_p}{r^3 k_B} - \frac{4\pi G\mu m_p \rho}{k_B}. \quad (7)$$

Before the second collapse occurs, there is no singularity at the center, and thus we use the boundary conditions

$$\rho(r=0) = \rho_0 \quad \text{and} \quad \frac{d\rho}{dr}(r=0) = 0, \quad (8)$$

where ρ_0 , the central density, remains a free parameter to be specified.

Figure 6 shows some examples of the density profile (upper panel) and integrated core mass (lower panel). The cases $\gamma = 5/3$ (blue), $\gamma = 4/3$ (cyan), and full eos (red) are plotted with $n_{\text{ad}} = 10^{10} \text{ cm}^{-3}$ (solid) and 10^9 cm^{-3} (dashed), where the legends correspond to the labels of the simulations. The black curves display the isothermal case. We also show the profile calculated with the eos used by Bate et al. (2003) with $\gamma = 7/5$ and $n_{\text{ad}} = 2.45 \times 10^{10} \text{ cm}^{-3}$. The central density used as boundary

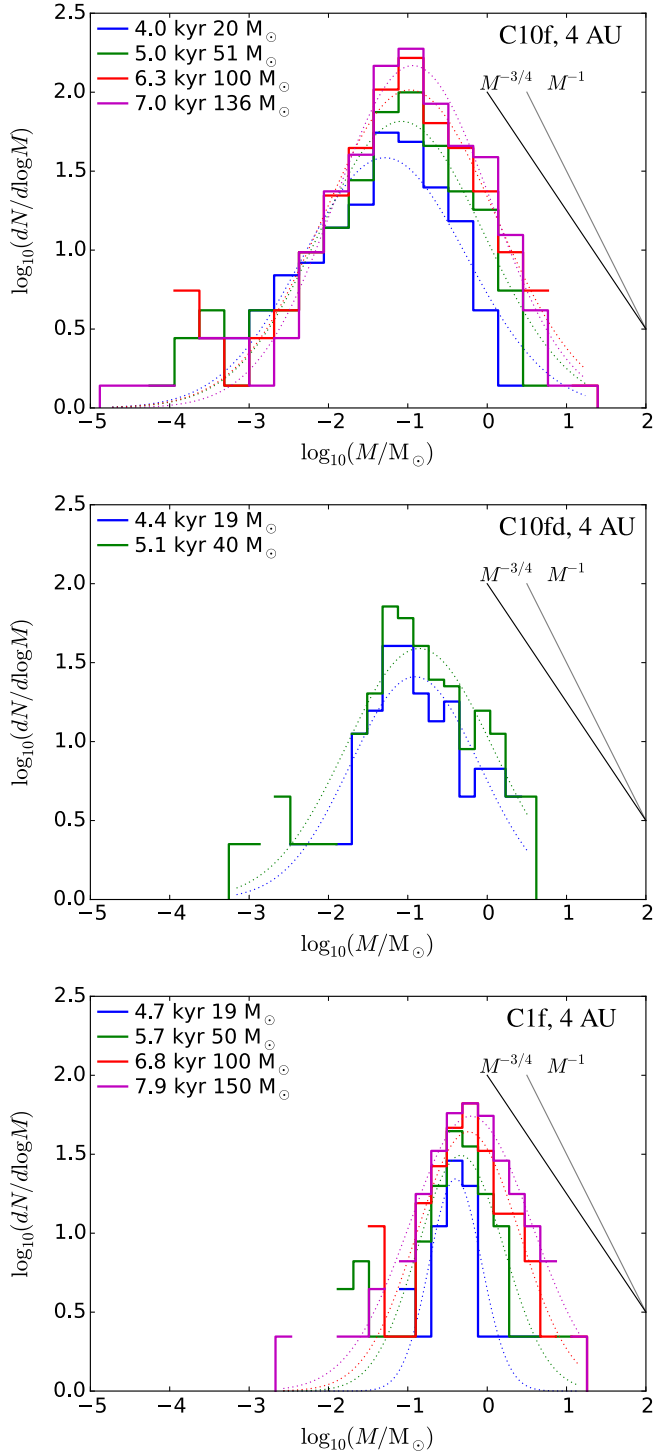


Fig. 5. Stellar distributions of runs with a full eos with $n_{\text{ad}} = 10^{10} \text{ cm}^{-3}$ (C10f, C10fd) and 10^9 cm^{-3} (C1f). The transitions to $\gamma = 5/3, 7/5$, and 1.0 occur at $n_{\text{ad}}, 30 n_{\text{ad}}$, and $30000 n_{\text{ad}}$. Using a higher sink density threshold (C10fd) results in fewer low-mass stars but does not change the peak of the stellar distribution. Decreasing n_{ad} by a factor ten increases the peak mass by ~ 10 .

condition for the integration was chosen to be $n_0 = 100 n_{\text{ad}}$, which is a reasonable value for illustrative purpose, while the actual value of n_0 that is reached in simulations depends on the resolution and sink formation algorithms.

In general, the result of the hydrostatic equilibrium without singularity is a central density plateau with a decreasing envelope. Depending on the central density, the solution may

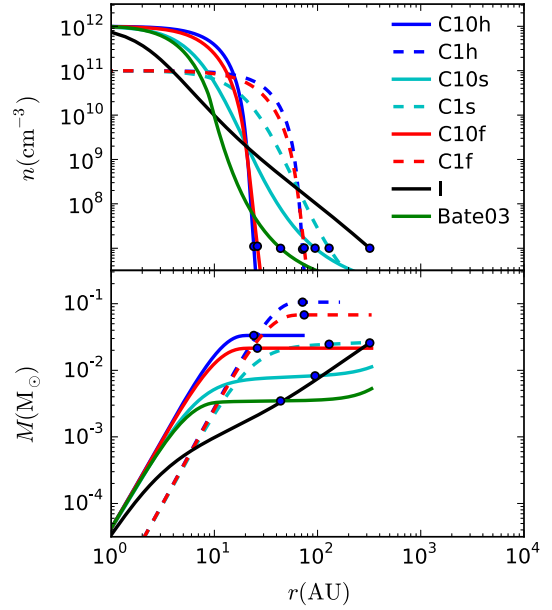


Fig. 6. First Larson cores for various equations of state. The hydrostatic equilibrium equations are integrated with $n_0 = 100 n_{\text{ad}}$ as boundary condition. We present cases with $\gamma = 5/3$ (blue), $\gamma = 4/3$ (cyan), full eos (red), and isothermal (black). The legends correspond to the labels of the simulations, with solid lines for $n_{\text{ad}} = 10^{10} \text{ cm}^{-3}$ and dashed lines for $n_{\text{ad}} = 10^9 \text{ cm}^{-3}$. We also show the case $\gamma = 7/5$ with $n_{\text{ad}} = 2.45 \times 10^{10} \text{ cm}^{-3}$ by Bate et al. (2003, green). The values of n_0 are chosen for illustrative purpose, and the actual values reached in simulations depend on the resolution (highest density resolved, see Fig. 7). The circle indicates the radius at which the density reaches 10^7 cm^{-3} , a reference ambient density that truncates the core. As long as the density profile decreases steeply enough, the choice of this truncation density has no strong effect on the resulting mass.

decrease infinitely or reach negative values at large radius, while it should be connected to a confining ambient pressure in physical conditions. For sake of convenience, we defined the boundary of this object where the density reaches the ambient density, namely 10^7 cm^{-3} in this study. With a sharply decreasing density profile, this selection of the density cutoff does not have a strong effect on the derived mass. As long as the outer density profile has a radial dependence that is much steeper than r^{-2} , the object is clearly distinguishable from the isothermal envelope and its mass is well defined.

Figure 7 displays the size of the core truncated at ambient density 10^7 cm^{-3} (top), the local power-law exponent of the density profile (middle) $\alpha = -rdn/dr/n$, such that locally $n \propto r^{-\alpha}$, with the gray line tracing $\alpha = 2$, and the integrated mass (bottom), as a function of the central density, n_0 , with several n_{ad} and γ values corresponding to the simulations. Above a certain value of n_0 (when the adiabatic regime begins), α starts to be significantly larger than 2 and a core is well defined, providing a clear definition of the first Larson core mass, M_L . Exceeding this mass, the gas becomes gravitationally bound, and this corresponds to the formation of sink particles in simulations. With low values of n_0 , on the other hand, the integrated mass is sensitive to the ambient density cutoff and is almost constant regardless of n_0 . This corresponds to the isothermal regime of the eos, and the density profile approaches that of a singular isothermal sphere (SIS; Shu 1977). The mass depends on the density cutoff, and no obvious core could be identified. The size is therefore physically meaningful only at high n_0 , while at low n_0 , it is merely a truncation of the SIS. In practice, we used $\alpha \gg 2$ to infer the

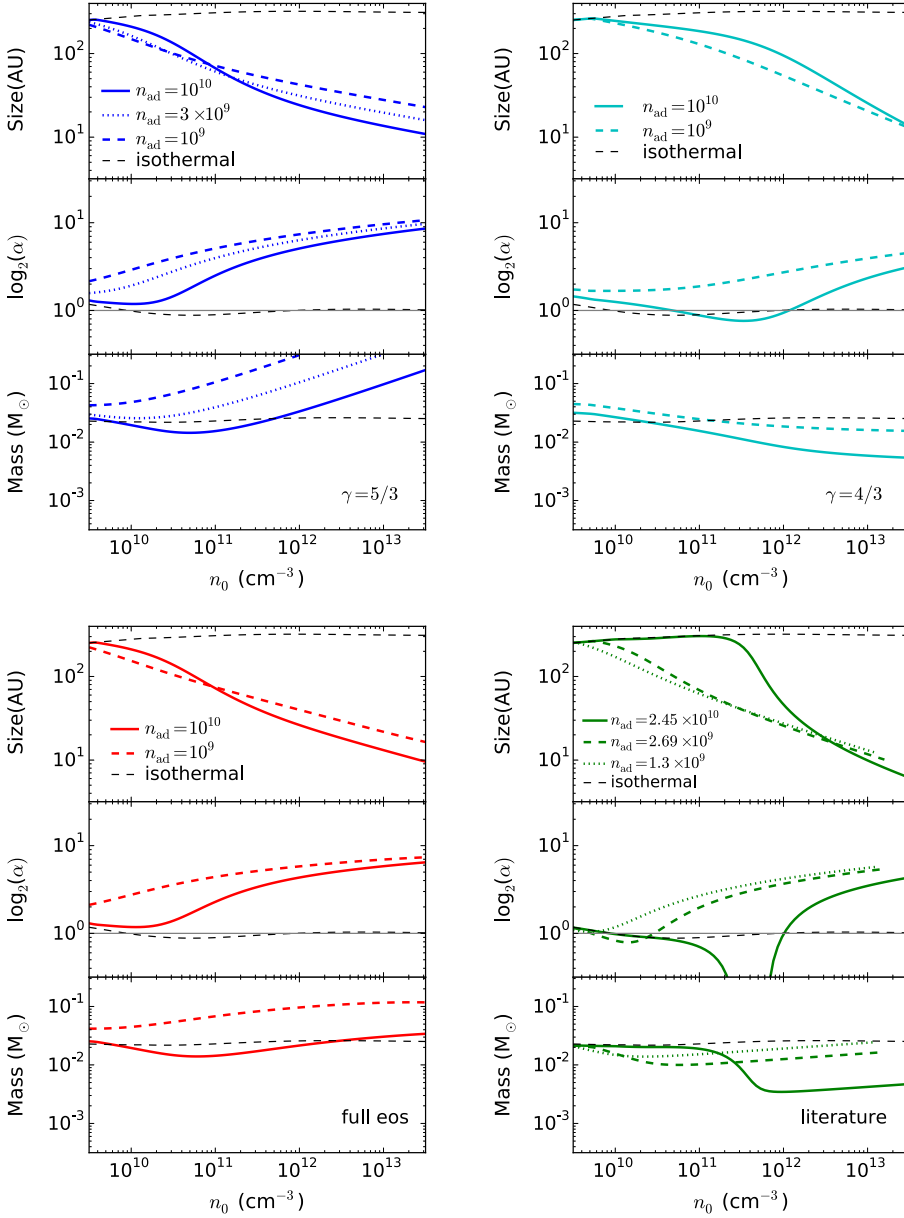


Fig. 7. Properties of the first Larson core plotted against the central density n_0 . The hydrostatic equilibrium Eq. (7) is solved with various n_{ad} and γ values, and truncated at the ambient density $n = 10^7 \text{ cm}^{-3}$. Three quantities are shown: the radius at which the density decreases to $n = 10^7 \text{ cm}^{-3}$, the local power law exponent $\alpha = -rdn/dr/n$, and the integrated mass. *Top left:* $\gamma = 5/3$; *top right:* $\gamma = 4/3$; *bottom left:* full eos. *Bottom right:* eos taken from Bate et al. (2003, solid), Bate (2005, dashed), and Bonnell et al. (2011, dotted). Each time the isothermal case is plotted in black for comparison. A core is well defined only when $\alpha \gg 2$, and thus giving a characteristic mass of the first Larson core. When a core is well defined, its mass is almost constant regardless of n_0 when $\gamma = 4/3$ or full eos is used. In contrast, the core mass increases with increasing n_0 when $\gamma = 5/3$, which explains the peak mass shift between runs C1h– and C1h–.

radius of the Larson core. As can be seen, the size of the first Larson core is typically a few tens of AU, well resolved in our simulations. When a non-isothermal eos is used, the density is almost flat at the center and significantly drops at some radius. The higher the value of n_0 , the smaller the size of the core, such that the integrated mass does not increase strongly with increasing n_0 , and even reaches a characteristic value, except for the cases with $\gamma = 5/3$, where the mass increases with n_0 at rate of roughly $M_L \propto n_0^{1/2}$.

An interesting question is whether rotation could modify these conclusions. In particular, since rotation adds another support, it might lead to more massive first Larson cores. To investigate this possibility, we used the ESTER code (Espinosa Lara & Rieutord 2013; Rieutord & Espinosa 2013), which computes bidimensional equilibria of rotating polytropes in solid-body rotation. We found that the maximum mass of a rotating polytrope increases only slightly (tens of percents). The reason is that the rotation support is significant only in the outer part, while most of the mass lies in the central region.

4.2. Interpreting the numerical simulation results

When we assume, as we show below, that the peak of the stellar distribution is simply proportional to the mass of the first Larson core, M_L , these calculations can be used to interpret the results obtained from the numerical simulations.

For $\gamma = 5/3$ and $n_{\text{ad}} = 10^{10} \text{ cm}^{-3}$, Fig. 2 shows that the peak of the stellar distribution does not change significantly with the resolution. Since increasing the resolution allows us to probe higher densities, we can interpret this behavior as a consequence of the weak dependence of M_L on the core central density, n_0 , which, as Fig. 7 shows (blue solid lines) remains below $2 \times 10^{-2} M_\odot$ for $n_0 < 10^{12}$, while noting that a self-gravitating core is well defined only when $n_0 \gtrsim 2 \times 10^{10}$ ($\alpha \gg 2$). With even higher resolution, we can expect that the peak of the stellar mass spectrum shifts to higher values, as seen with the C1h runs at varied resolutions.

For $n_{\text{ad}} = 10^9 \text{ cm}^{-3}$ and $\gamma = 5/3$ (Fig. 3), the self-gravitating first Larson core is always well defined, with a mass that increases with n_0 . This is reflected by the shift in peak mass

between runs C1h– – and C1h–. The eos with $n_{\text{ad}} = 10^9 \text{ cm}^{-3}$ gives a mass of the first Larson core that is higher than that with $n_{\text{ad}} = 10^{10} \text{ cm}^{-3}$ at the same value of n_0 , which is also in agreement with simulation results.

With $\gamma = 4/3$, the effect of varied n_{ad} on the peak of the stellar distribution was found to be less significant (Fig. 4). This is again in good agreement with Fig. 7 (cyan lines), where at the same value of n_0 , the mass varies less with n_{ad} than in the $\gamma = 5/3$ cases.

Finally, the runs with full eos (Fig. 5) present a similar behavior to the runs with $\gamma = 5/3$ (Fig. 3) regarding the relation between peak mass and n_{ad} . This is also expected as the mass dependence of M_{L} is relatively similar to that of $\gamma = 5/3$ for n_0 below 10^{12} cm^{-3} (Fig. 7, red lines).

4.3. Correlation between the first Larson core and the stellar distribution peak

A link between the mass of the first Larson core, M_{L} , and the mass at which the stellar distribution peaks has been suggested in previous discussions. We now compare this in a more systematic way. For this purpose, we have compiled our simulations with other results from the literature, and we present in Fig. 8 the correlation between the peak mass of the stellar distribution and the mass of the first Larson core deduced from the eos we employed in the corresponding runs. The mass of the first Larson core is deduced from Fig. 7 to lie around the point where α starts to be larger than two. Since the definition is not entirely straightforward and also because M_{L} depends on n_0 , we estimated error bars by considering that n_0 may vary by a factor 10. To estimate the peak position, we took the mass corresponding to the maximum values in the mass spectra. The error bars are given by the binning size.

We also included results from literature. Bate et al. (2003) simulated a $50 M_{\odot}$ cloud with $\gamma = 7/5$ above $10^{-13} \text{ g cm}^{-3}$ and obtained a median sink mass of $0.7 M_{\odot}$. Increasing the density by decreasing the size (Bate & Bonnell 2005) or increasing the mass and velocity dispersion while keeping the same density (Bate 2009a) gave similar median masses of 0.023 and $0.02 M_{\odot}$ that are significantly lower than in the previous case. Alternatively, changing the critical density to $1.1 \times 10^{-14} \text{ g cm}^{-3}$ (Bate 2005) gave a median mass of $0.054 M_{\odot}$. The median mass was used from these studies since there is not enough statistics and a peak was not always well defined. The eos used in the simulation series by Bate et al. is a piece-wise temperature. To calculate the density profile of a mass concentration, the temperature as well as its derivative are required to be continuous, therefore we used

$$T = T_0 \left[1 + (\rho/\rho_{\text{ad}})^{(\gamma-1)n} \right]^{1/n}, \quad (9)$$

where $n = 100 \gg 1$, to replace their eos when we inferred the mass of the first Larson core.

Figure 8 shows that the first Larson core mass is in good correlation with the stellar distribution peak, and we approximately obtain $M_{\text{peak}} \approx 10 M_{\text{L}}$. We offer an explanation for this additional factor of about ten in Sect. 5.

5. Stabilizing effects of tidal forces around the first Larson core: a model

To link the mass of the first Larson core to the mass of the forming star, we present a simple model to discuss the effect of a point mass in a density field. The questions we address are

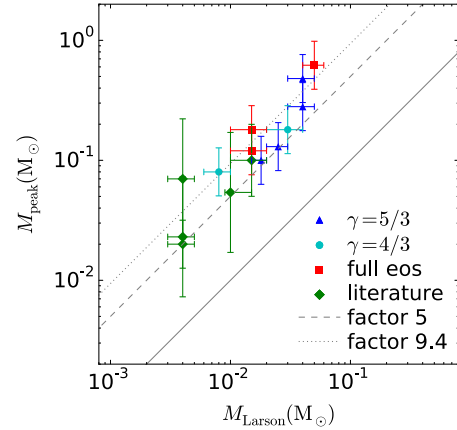


Fig. 8. Peak mass of the sink mass spectrum plotted against the mass of the first Larson core calculated with the eos we used in the simulations. The peak mass is read from the stellar distribution, with the bin size as error. The error bars from literature results are larger as they have lower statistics and higher fluctuations in the spectrum. The mass of the first Larson core is read from Fig. 7, with error bars indicating the mass range with the probable n_0 range. When we examine this by eye, there is a correlation $M_{\text{peak}} \sim 5 M_{\text{Larson}}$. We also performed a simple linear regression, without considering the errors, to determine the scaling factor, and this led to $\sum(M_{\text{peak}} M_{\text{Larson}}) / \sum M_{\text{Larson}}^2 = 9.4$.

how the typical mass of a self-gravitating object embedded in a dense collapsing cloud is limited in general to a small fraction of that of this cloud, and how this fraction depends on the mass of the accreting object. Here we propose that the accretion onto the already formed self-gravitating object competes with the tendency to form new objects from gravo-turbulent fragmentation. We therefore wish to estimate the typical radius at which the probability to form another self-gravitating fragment equals one. The mass enclosed within this radius is expected to be accreted by the central object, while the mass outside is expected to be distributed between forming fragments.

We discuss the conditions under which a density perturbation located near the point mass can become self-gravitating and form another core. The idea is that the first Larson core will “screen” itself by shearing out fluctuations through tidal forces. The modeling essentially proceeds in four steps:

- In Sect. 5.1 we describe a point mass that is surrounded by a density profile, with a perturbation at distance r_p and of size δr .
- In Sect. 5.2 we develop the mass condition. The perturbation needs to have a mass of at least M_{L} such that its collapse can result in the formation of a stellar object.
- In Sect. 5.3 we infer the energy condition. The gravitational field generated by the point mass, the density field, and the perturbation itself are used to calculate the gravitational energy of the perturbation. The idea is to compare the self-gravity of the perturbation to the destructive tidal field created by the point mass and the envelope. The gravitational energy of the perturbation is required to be negative such that it can contract to form another star.
- In Sect. 5.4 we estimate the mass that is expected do eventually be accreted onto the central object. The mass and energy constraints provide a condition on the density perturbations as a function of distance. Assuming a lognormal distribution for the density fluctuations (in addition to the local mean density, which itself is $\propto r^{-2}$), we can infer at which radius the probability of finding a self-gravitating perturbation of mass at least equal to M_{L} is one.

5.1. Step 1: density profile around sink particles and perturbation

By extracting gas profiles around young sinks particles that have not yet decoupled from their natal gas, we have shown in Paper I that the cores that form stars have indeed some characteristic density profiles $\rho \propto r^{-2}$, as expected from theory (Shu 1977). We therefore take the density field $\rho_e(r_e)$ as a function of distance to the point mass

$$\rho_e = \frac{Ac_s^2}{2\pi G} \frac{1}{r_e^2}, \quad (10)$$

where A is the amplitude of the SIS density profile (Shu 1977). In Paper I, the density profiles around young sink particles were inferred from simulations, and a typical value of $A \sim 10$ was found at early time when the sinks are still actively accreting (see the left panels of Fig. 4 of Paper I). For the sake of simplicity, we consider a uniform density spherical perturbation ρ_p at distance r_p :

$$\rho_p = \eta \frac{Ac_s^2}{2\pi G} \frac{1}{r_p^2} \text{ for } |\mathbf{r}_e - \mathbf{r}_p| = |\delta\mathbf{r}| = \delta r \leq \delta r_p, \quad (11)$$

where \mathbf{r}_e and \mathbf{r}_p are the vectors pointing from the central object to a point in the envelope and to the center of perturbation, and η is a constant for the local density contrast of the perturbation.

To determine whether the perturbation is prone to self-gravitating collapse, we use the virial theorem to probe its stability

$$\begin{aligned} E_{\text{vir}}(r_p, \delta r_p, \eta) &= E_g(r_p, \delta r_p, \eta) + 2E_{\text{ther}} \\ &= \int_{V_p} \rho \mathbf{g} \cdot \delta \mathbf{r} \, dV + 3M_p(r_p, \delta r_p, \eta)c_s^2 \\ &= \int_{V_p} (\rho_e + \rho_p) (\mathbf{g}_L + \mathbf{g}_e + \mathbf{g}_p) \cdot \delta \mathbf{r} \, dV + 3M_p(r_p, \delta r_p, \eta)c_s^2. \end{aligned} \quad (12)$$

The virial energy E_{vir} is a combination of the gravitational energy E_g and the thermal energy E_{ther} , with M_p being the mass of the perturbation. The gravitational acceleration $\mathbf{g} = \mathbf{g}_L + \mathbf{g}_e + \mathbf{g}_p$ has three components, coming from the central first Larson core that is described with a point mass, the power-law density envelope, and the perturbation itself. We note that to correctly calculate the virial energy, only the tidal tensor part of the gravity should be considered and the mean value exerted on the center of the object should be removed. In the following, we therefore always use the relative gravitational acceleration with respect to the center of the perturbation. The collapse criteria are therefore

$$M_p(r_p, \delta r_p, \eta) \geq M_L \quad \text{and} \quad (13)$$

$$E_{\text{vir}}(r_p, \delta r_p, \eta) \leq 0. \quad (14)$$

5.2. Step 2: the mass condition

The mass contained inside the perturbation radius δr_p around the center of perturbation is

$$M_p(r_p, \delta r_p, \eta) = \int_{V_p} \rho(\mathbf{r}_e) \, dV = \int_{V_p} (\rho_e + \rho_p) \, dV. \quad (15)$$

We designate θ the angle between $\delta \mathbf{r}$ and $-\mathbf{r}_p$. With the trigonometric relation

$$r_e^2 = r_p^2 + \delta r^2 - 2r_p \delta r \cos \theta, \quad (16)$$

we can integrate

$$M_p(r_p, \delta r_p, \eta) = \frac{Ac_s^2}{G} r_p m_p(u_p, \eta), \quad (17)$$

where the normalized quantity $u_p = \delta r_p / r_p$. The normalized mass is expressed as $m_p(u_p, \eta)$ and is given in Appendix B.

As explained above, the mass of the perturbation must typically be equal to M_L since no star can form below this value. By requiring $M_p(r_p, \delta r_p, \eta) = M_L$, we obtain a relation between the size u_p and amplitude η of a perturbation at distance r_p .

5.3. Step 3: the energy condition

Now turning to the calculation of the virial parameter, we first show the importance of tidal forces in the vicinity of the sink particles, and then, to gain physical intuition, we perform a simplified 1D estimate before carrying out a full 3D calculation.

5.3.1. Tidal forces

Tidal forces have been advocated in various contexts to either limit or quench star formation (Bonnell & Rice 2008; Ballesteros-Paredes et al. 2009), but also, conversely, to trigger it (Jog 2013; Renaud et al. 2014). Ntormousi & Hennebelle (2015) discussed the influence of the density distribution and showed that in a collapsing cloud, the tidal forces tend to be initially compressive, which promotes fragmentation, and then the forces become stabilizing. The key quantity to study the influence of tidal forces is the gravitational stress tensor, $\partial_i g_j$, which is characterized by the three eigenvalues, λ_i . From the Poisson equation, we know that $\sum \lambda_i = -4\pi G\rho$. Thus there is at least one negative eigenvalue, say λ_1 , and in most cases, two of them are negative. It is well known that certain gravitational fields present a value of λ_3 that is positive and that these fields render the formation of self-gravitating perturbations less likely (see Appendix C for the tidal forces in the simulation). Below, the tidal effect is taken into account by including the corresponding term in the virial theorem.

5.3.2. 1D calculation of gravitational energy

The direction along \mathbf{r}_p is the relevant dimension as the gravity of the central mass, and the envelope generates diverging tidal forces and prevents the overdense perturbation from self-gravitating collapse. Based on the reasonable illustrative results and for simplicity, we first perform a virial integration along this direction on the axis of the perturbation, ignoring thermal energy, and try to obtain some physical insight from the simplified calculations. We define the position δr with respect to the center of perturbation at r_p , with the positive direction pointing away from the central mass. The gravitational acceleration, relative to the center of the perturbation, along the radial direction is

$$g(\delta r) = -\frac{GM_L}{(r_p + \delta r)^2} + \frac{GM_L}{r_p^2} - \frac{2Ac_s^2}{r_p + \delta r} + \frac{2Ac_s^2}{r_p} - \eta \frac{2Ac_s^2}{3r_p^2} \delta r. \quad (18)$$

By removing the acceleration in the moving coordinate of the perturbation, the tidal force generated by the gravity is adequately considered. The first two terms on the right-hand side

represent the gravitational acceleration generated by the central star, the third and fourth terms are the acceleration by the envelope, and the last term is the gravity of the perturbation itself. The density is

$$\rho(\delta r) = \frac{Ac_s^2}{2\pi G} \left(\frac{1}{(r_p + \delta r)^2} + \frac{\eta}{r_p^2} \right). \quad (19)$$

The virial integration therefore is

$$\int_{-\delta r_p}^{\delta r_p} \rho(\delta r) g(\delta r) \delta r d\delta r = \frac{(Ac_s^2)^2}{2\pi G r_p} \mathcal{E}_{1D,g}(r_p, u_p, \eta), \quad (20)$$

where $\mathcal{E}_{1D,g}$ is the non-dimensionalized energy (a detailed derivation is given in Appendix D). This is a line integration, and the quantity has the dimension of energy per unit surface. We define a normalizing radius

$$r_L = \frac{GM_L}{2Ac_s^2} = 1.1 \times 10^2 \text{ AU} \left(\frac{1}{A} \right) \left(\frac{M_L}{0.01 M_\odot} \right), \quad (21)$$

such that

$$\tilde{r}_p = r_p/r_L = M_e(r_p)/M_L, \quad (22)$$

where $M_e(r_p) = 2Ac_s^2 r_p/G$ is the mass of the envelope within r_p . The energy $\mathcal{E}_{1D,g}$ can be expressed as

$$\mathcal{E}_{1D,g}(\tilde{r}_p, u_p, \eta) = \frac{2}{\tilde{r}_p} \mathcal{E}_{1D,L}(u_p, \eta) + \mathcal{E}_{1D,e}(u_p, \eta) + \mathcal{E}_{1D,p}(u_p, \eta), \quad (23)$$

with contributions from the three components.

The solutions are found by simultaneously solving for all \tilde{r}_p

$$m_p(u_p, \eta) = \frac{2}{\tilde{r}_p} \quad \text{and} \quad \mathcal{E}_{1D,g}(\tilde{r}_p, u_p, \eta) = 0. \quad (24)$$

The first condition is the condition stated by Eq. (13), while the normalized expression stated by Eq. (17) is used.

We plot the critical density contrast η_c and the corresponding size of the perturbation, $\tilde{\delta r}_p = \delta r_p/r_L$, against \tilde{r}_p in Fig. 9, showing that with increasing distance from the central star, a lower density contrast (smaller η) and a lower level of mass concentration (larger δr_p) are needed for the perturbation to be self-gravitating. As η increases at fixed mass, u_p and $\mathcal{E}_{1D,g}(\tilde{r}_p, u_p, \eta)$ decrease. At any given distance to a first Larson core, we can therefore derive a critical local density contrast η_c above which the perturbation is self-gravitating and is prone to collapse. Within this distance, all density fluctuations lower than η_c are prevented from collapsing by the tidal field of the central mass and its envelope. The value of η_c is typically higher than a factor of a few, while the radius of the perturbation must be significantly smaller than the distance from the central object. These numbers indicate that the conditions for a perturbation to become unstable are not easy to satisfy, and most perturbations that in the absence of tidal forces would be unstable are therefore rendered stable. This process favors further accretion onto the central object other than distributing the mass between new fragments.

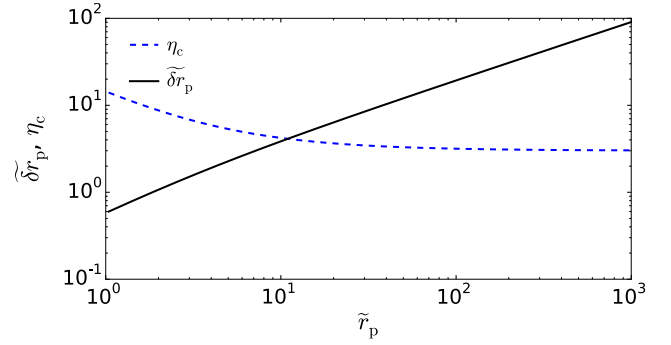


Fig. 9. Critical value of η_c (blue dashed) and corresponding $\tilde{\delta r}_p$ (black solid) as functions of the normalized distance \tilde{r}_p . The gravitational potential energy is calculated in 1D.

5.3.3. Full 3D calculation

The SIS density profile generates a positive tidal force in the radial direction, while the field is compressing in the other two directions. A full 3D calculation can therefore be different from the 1D case, and it is necessary to clarify this effect. For conciseness, the full integration of Eq. (12) in 3D space is presented in Appendix E, and here we simply discuss the results:

$$\begin{aligned} E_g(r_p, \delta r_p, \eta) &= \frac{(Ac_s^2)^2}{G} r_p \mathcal{E}_{3D,g}(\tilde{r}_p, u_p, \eta) \\ &= \frac{(Ac_s^2)^2}{G} r_p \left[\frac{2}{\tilde{r}_p} \mathcal{E}_{3D,L}(u_p, \eta) \right. \\ &\quad \left. + \mathcal{E}_{3D,e}(u_p, \eta) + \mathcal{E}_{3D,p}(u_p, \eta) \right], \end{aligned} \quad (25)$$

where $\mathcal{E}_{3D,g}$ is the normalized gravitational energy. The results are qualitatively similar to the 1D calculations. The values of η_c and corresponding $\tilde{\delta r}_p$ are plotted in Fig. 10 as a function of the normalized distance \tilde{r}_p (magenta). At a short distance, they are very similar to the 1D approximation and η_c must be larger than several, but at a large distance, η_c drops to ~ 1 , implying that the perturbation is easily unstable.

However, we also need to consider the thermal support $3M_p c_s^2$ against self-gravity. We can infer the condition $\mathcal{E}_{3D,g} + 3m_p/A \leq 0$ from Eqs. (12) and (17). Including the thermal support does not change the conclusions at small r_p much, while at larger distance, where the envelope density is low, thermal support becomes dominant and tidal forces are unimportant. In this context, η_c becomes an increasing function of r_p , thus imposing a lower limit on η_c (black lines in Fig. 10).

The result sensitively depends on A , the amplitude of the density field. When A is equal to a few, the combination of thermal support and tidal forces stabilizes most perturbations. Only fluctuations denser than about ten times the background density can eventually collapse. This is in good agreement with simulations such as those performed by Girichidis et al. (2011), which show that clouds with r^{-2} density profiles are not prone to fragmentation.

5.4. Step 4: final mass from the integrated probability of the formation of a nearby first Larson core

In the previous section we obtained the critical density contrast, η_c , for forming a second self-gravitating core near a point mass M_L as a function of the distance. The question now is under which circumstances would such fluctuations be encountered, or

more precisely, what is the probability for a given perturbation amplitude to occur? To answer this question, we need to know the fluctuation spectrum within a collapsing clump around an accreting point mass. Since there is no available statistics, this last step is certainly the least quantitative. To obtain some estimate, we now use the typical density fluctuations produced by supersonic turbulence to determine the characteristic distance at which a perturbation with sufficient amplitude could be found and a second core could form. The mass within this radius is expected to be protected from fragmentation and therefore should be accreted.

We use the simple assumption of a lognormal PDF (e.g., Vázquez-Semadeni 1994; Federrath et al. 2008; Hennebelle & Falgarone 2012), that is, the probability of finding perturbations of η at distance \tilde{r}_p is

$$P(\tilde{r}_p, \delta) = \frac{1}{\sqrt{2\pi}\sigma(\tilde{r}_p)} \exp\left[\frac{-(\delta + \sigma^2(\tilde{r}_p)/2)^2}{2\sigma^2(\tilde{r}_p)}\right], \quad (26)$$

where $\delta = \log(1 + \eta)$ and σ is the width of the density PDF. The density fluctuation is related to the local turbulent Mach number such that $\sigma^2(\tilde{r}_p) = \log(1 + b^2 \mathcal{M}(\tilde{r}_p)^2)$, with $b = 0.5$. To estimate the local Mach number, we assume that the turbulent Mach number is proportional to the that obtained from the infall velocity. This implies that the collapse is able to amplify existing perturbations until local energy equipartition is reached. Given the mass of the central core and the envelope, the turbulent Mach number therefore is

$$\begin{aligned} \mathcal{M}(\tilde{r}_p) &= \frac{1}{c_s} \sqrt{\frac{G[M_L + M_e(r_p)]}{r_p}} \epsilon = \frac{1}{c_s} \sqrt{\frac{GM_L(1 + \tilde{r}_p)}{r_p}} \epsilon \\ &= \sqrt{2A(1 + \frac{1}{\tilde{r}_p})} \epsilon, \end{aligned} \quad (27)$$

where the second equivalence is obtained using Eq. (22) and the third using Eq. (21). The coefficient, $\epsilon \leq 1$, represents the amount of released gravitational energy that goes into the turbulent fluctuations, rather than the infalling component. As estimated in Paper I, $A \simeq 10$, leading to $\mathcal{M} \simeq 4\sqrt{\epsilon}$. We refer to this assumption as model I. We integrate the mass that exceeds the critical density at all r_p , using the density of the fluctuation $\rho(\tilde{r}_p) \exp(\delta)$, the local background multiplied by the relative density fluctuations. Dividing by M_L , we obtain the typical number of self-gravitating cores with a mass at least equal to M_L contained within r_p

$$\begin{aligned} \mathcal{N}(\tilde{r}_p) &= \frac{1}{M_L} \int_0^{\tilde{r}_p} \int_{\delta_c}^{\infty} P(\tilde{r}_p, \delta) \rho(\tilde{r}_p) \exp(\delta) 4\pi r_p'^2 d\delta dr_p' \\ &= \int_0^{\tilde{r}_p} \frac{1}{2} \left[1 + \operatorname{erf}\left(\frac{\sigma^2(\tilde{r}_p) - 2\delta_c}{2\sqrt{2}\sigma(\tilde{r}_p)}\right) \right] \frac{Ac_s^2}{2\pi G r_p'^2} \frac{4\pi r_p'^2}{M_L} dr_p' \\ &= \int_0^{\tilde{r}_p} \frac{1}{2} \left[1 + \operatorname{erf}\left(\frac{\sigma^2(\tilde{r}_p) - 2\delta_c}{2\sqrt{2}\sigma(\tilde{r}_p)}\right) \right] d\tilde{r}_p', \end{aligned} \quad (28)$$

where we have used Eq. (21) to normalize the expression. With the definition of \tilde{r}_p , the mass contained within a sphere of radius $a\tilde{r}_p$ is equal to aM_L . When $\mathcal{N}(\tilde{r}_p^*) = 1$, the probability of getting

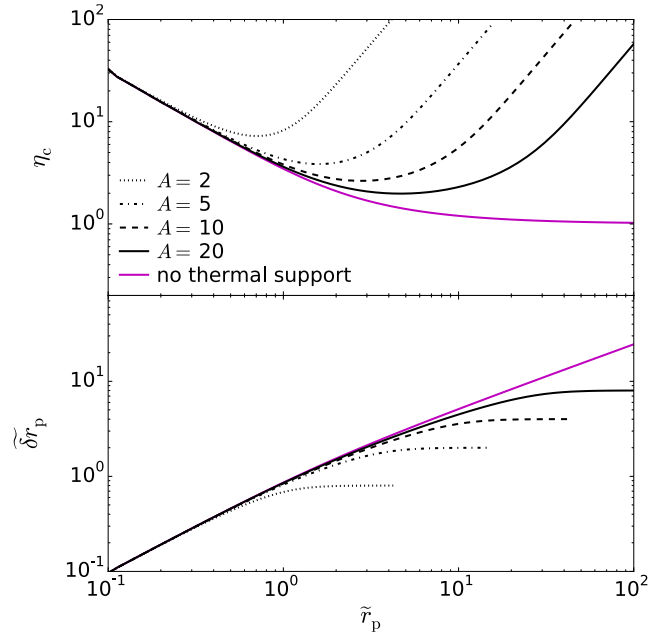


Fig. 10. Critical value of the perturbation amplitude, η_c (upper panel) and corresponding normalized size of the perturbation $\delta\tilde{r}_p$ (lower panel) as a function of the normalized distance \tilde{r}_p . 3D gravitational energy is used, and thermal support is included for various density profiles. Fluctuations have to be at least several times the local density to be unstable. The low-amplitude perturbations are stabilized by tidal forces or thermal support.

another fragment with mass M_L is equal to 1. The mass enclosed within this radius is accreted by the central object since this mass is protected from fragmentation. Thus the mass of the final object is certainly higher than $M_F = (1 + \tilde{r}_p^*)M_L$.

Figure 11 shows M_F as a function of A . The typical values of $A \sim 10$ – 20 and $\epsilon \sim 0.5$ give a final stellar mass of $\sim 4 M_L$ when we integrate up to $\mathcal{N} = 1$ (black lines), ~ 8 – 9 or 20 – $30 M_L$ is obtained when we consider $\mathcal{N} = 3$ (blue lines) or $\mathcal{N} = 10$ (cyan lines). Up to which radius should be integrated, that is to say, how far the protostar is able to accrete, is a difficult question. Typically, we can estimate that about six fragments (one for each direction) should prevent any further accretion, but on the other hand, these fragments will attract mass that should not be attributed to the central object. Therefore, three fragments sounds like a reasonable number. In Appendix F we explore another model for the Mach number dependence, which leads to similar conclusions.

We recall that the mass is integrated without considering whether the masses are spatially connect. The value of \mathcal{N} is thus a lower limit, and so is the derived \tilde{r}_p^* . Although the model we presented is not very accurate, it nevertheless suggests that the nonlinear factor of $\simeq 10$ inferred from the simulations is entirely reasonable. Further work is certainly required here.

5.5. Tidal protection in simulations

To verify our model of tidal protection that inhibits nearby core formation, we examined the distance between the sinks in our simulations. For each sink, the distance of formation position was calculated for all younger sinks. In Fig. 12 we plot the distances of the first and tenth closest neighbors against the instantaneous sink mass at the moment of neighbor formation for run C10h+. The distances of the first few closest sinks are similar and almost identical in most cases (which suggests that our

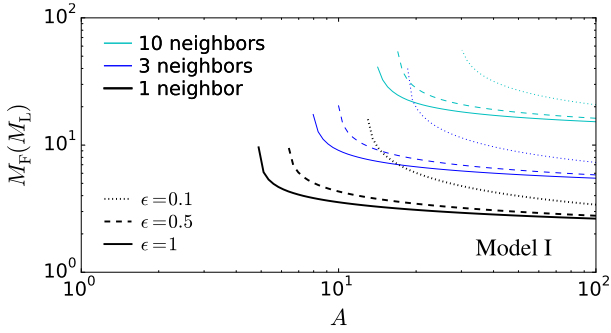


Fig. 11. Final mass M_F , in units of M_L , plotted against A , the amplitude of the density envelope (Eq. (10)), and for various ϵ , the efficiency at which infall triggers turbulent fluctuations. The critical radius \tilde{r}_p^* is equivalent to the amount of protected envelope mass in units of M_L , and thus $M_F = (\tilde{r}_p^* + 1)M_L$. Black lines show the expected mass when the envelope is truncated at $\mathcal{N}(\tilde{r}_p) = 1$, and M_F is expected to be larger than 4 for typical values of A . Blue thin lines show the same result, while truncated at $\mathcal{N}(\tilde{r}_p) = 3$, and the expected M_F is increased to ~ 8 – 9 . Cyan lines show results for $\mathcal{N}(\tilde{r}_p) = 10$.

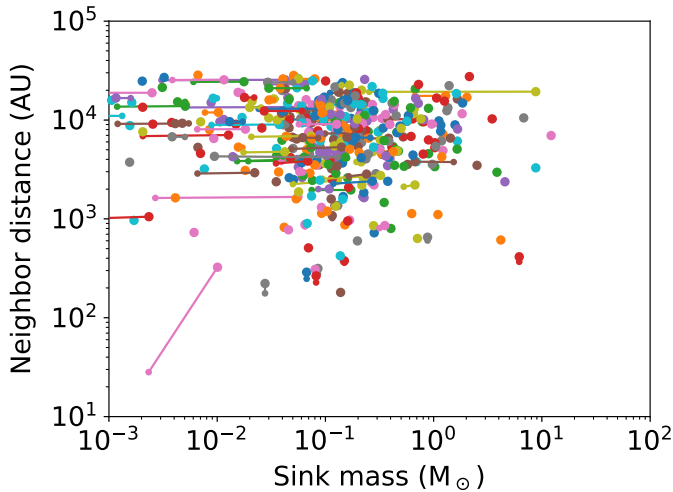


Fig. 12. Distance of nearby sink formation plotted against sink mass. The distance is calculated at the moment of the neighboring sink formation. The distances from the each sink to its first and tenth (small and large dots interlinked by a line) closest neighbors are plotted against its mass at the moment of the formation of the neighbors. Around an existing sink particle, any neighbor can hardly form within the distance of a few hundreds of AU.

model needs further refinement). The formation of a nearby sink is generally inhibited within the distance of several hundreds of AU for established sinks.

6. Discussions

6.1. Necessary developments

In our simulations, the physics of the first Larson core sets the peak of the stellar distribution, and we infer $M_{\text{peak}} \approx 10 M_{\text{Larson}}$. The mass of the first Larson core at the point where it undergoes second collapse is typically on the order of a few $0.01 M_{\odot}$ (Masunaga et al. 1998; Vaytet et al. 2012; Vaytet & Haugbølle 2017), which is very close to the observed peak of the IMF (Bastian et al. 2010). The most recent radiative simulations of core collapse by Vaytet & Haugbølle (2017) showed that the mass of the first Larson core is $\sim 0.02 M_{\odot}$. One of the difficulties

encountered by our calculations is that it is not possible to properly describe the second collapse and the disappearance of the first Larson core as it is being accreted. This causes some uncertainties in the value of the first Larson core that should be used. A smoothed two-slope polytropic eos was used in this study to represent the results of radiative transfer balancing in dense gas. Detailed simulations with complete radiation calculations would give more accurate results, although the numerical resolution is a major obstacle. On the other hand, varying the density at which the sink particles are introduced (runs C10f and C10fd in Fig. 5) does not change the position of the peak, although it reduces the number of objects. This may indicate that the exact way in which the first core is accreted onto the protostar may be not too critical in determining the peak position.

Finally, we reiterate that the physics used in the present paper and its companion may be oversimplified in other aspects since it does not include the magnetic field and heating by accretion luminosity. Both are known to reduce fragmentation (Krumholz et al. 2007a; Bate 2009b; Commerçon et al. 2011; Hennebelle et al. 2011; Myers et al. 2013) and may drastically modify the fragmentation we obtain.

6.2. What sets the peak of the IMF: is there a cosmic conspiracy?

Unlike the prediction by simple gravo-turbulent fragmentation models (e.g., Hennebelle & Chabrier 2008, 2013; Hopkins 2012), which posit that the IMF peak depends on the turbulent Jeans mass, the IMF characteristic mass in the high-density regime has a lower limit imposed by the local thermal balancing and the formation of the first Larson core. The traditional view that the typical fragmentation mass is linked to the Jeans mass is no longer valid in these conditions because self-gravity triggers the development of a power-law density PDF. As discussed in Paper I, the existence of a peak may depend on the environment, however. In somewhat diffuse clouds, or more precisely, when the local thermal support dominates the turbulent support, the stellar distribution is flat ($dN/d \log M \propto M^0$) and the mass of the first Larson core, M_{Larson} , may truncate the distribution rather than leading to a peak.

One important issue, however, is the initial conditions and the exact way the matter is assembled. Although we verified in Paper I (see the appendix) that the initial fluctuations are not crucial, setting up a dense reservoir without preexisting cores may be a significant oversimplification. In other words, the initial conditions that should be used to describe the ISM are not well understood yet, and we caution that the conditions used in this paper may introduce some biases. In particular, as stressed in Paper I, the high-mass part of the mass spectra tends to present a power law that is too shallow compared to the canonical Salpeter distribution. If dense clusters turn out to be assembled from material where cores are already developed, the preexisting cores may play a stronger role and the peak of the IMF could be inherited from the peak of the core mass function (CMF), as proposed theoretically in Padoan et al. (1997), Hennebelle & Chabrier (2009), Hennebelle (2012), Hopkins (2012), Lee & Hennebelle (2016a), and Lee et al. (2017), and suggested by simulations (Gong & Ostriker 2015; Hennebelle 2018). This picture is suggested by the observations of the CMF, which resembles the IMF (Motte et al. 1998; Alves et al. 2007; André et al. 2010; Könyves et al. 2015), and it could be the dominant mode in some environments. It is remarkable that the peak of the CMF (particularly if an efficiency of ≈ 30 – 50% is taken into account) and the peak of the stellar distribution imposed by the physics of the first Larson

core, as discussed in this paper, lead to values that are similar within a factor of 2–3. This coincidence may be for a large part responsible of the apparent universality of the IMF.

7. Conclusions

We have performed a series of numerical simulations describing the collapse of a $1000 M_{\odot}$ cloud. These numerical experiments explicitly ignored magnetic field and radiative transfer at this stage. The transition from the isothermal to the adiabatic phase is of great importance, and several effective equations of state were explored. This includes varying γ , the effective adiabatic exponent, and ρ_{ad} , the density at which the transition occurs. We paid great attention to the numerical spatial resolution and its influences on the resulting stellar mass spectrum, in particular, its peak position. The influence of the initial conditions were studied in Paper I.

We found that the isothermal simulations show no sign of convergence as the peak position shifts toward lower masses when the spatial resolution improves. On the other hand, when a polytrope-like eos is used (typically with $\gamma > 4/3$), the peak position becomes independent of the numerical resolution if high enough. Using simple 1D hydrostatic models, we inferred the expected mass of the first Larson core that we compared to the measured peak position of the stellar distribution, for which we compared our simulations and various published results. We found a clear correlation between the two, with the peak position typically about ten times higher than the mass of the first Larson core.

We presented an analytical model that may account for this factor of roughly ten. It is based on the idea that in the vicinity of a point mass, such as a first Larson core, tidal forces are important and tend to quench further gravitational fragmentation by shearing out the density fluctuations. Therefore the mass located in the neighborhood of such a point mass tends to be accreted, which increases the mass of the central objects in consequence. As discussed in Paper I, this effect is true only when the gas is initially dense and turbulent, generating many fluctuations that eventually form stars close one to the other.

Since the physics of the first Larson core is not expected to significantly vary from place to place, this mechanism may provide a robust explanation for the apparent universality of the IMF peak. We emphasize, however, that an IMF-like distribution is produced only if the cloud is sufficiently massive and cold.

Acknowledgements. We thank the anonymous referee for comments that have improved the manuscript. We thank Gilles Chabrier for a critical reading of the manuscript. We thank Michel Rieutord for providing the ESTER code and helping us to run it to explore the influence of the rotation on the mass of a polytrope. This work was granted access to HPC resources of CINES under the allocation x2014047023 made by GENCI (Grand Equipement National de Calcul Intensif). This research has received funding from the European Research Council under the European Community's Seventh Framework Programme (FP7/2007-2013 Grant Agreement no. 306483). Y.-N. Lee acknowledges the financial support of the UnivEarthS Labex program at Sorbonne Paris Cité (ANR-10-LABX-0023 and ANR-11-IDEX-0005-02).

References

Alves, J., Lombardi, M., & Lada, C. J. 2007, *A&A*, 462, L17
 André, P., Men'shchikov, A., Bontemps, S., et al. 2010, *A&A*, 518, L102

Ballesteros-Paredes, J., Gómez, G. C., Loinard, L., Torres, R. M., & Pichardo, B. 2009, *MNRAS*, 395, L81
 Ballesteros-Paredes, J., Hartmann, L. W., Pérez-Goytia, N., & Kuznetsova, A. 2015, *MNRAS*, 452, 566
 Bastian, N., Covey, K. R., & Meyer, M. R. 2010, *ARA&A*, 48, 339
 Bate, M. R. 2005, *MNRAS*, 363, 363
 Bate, M. R. 2009a, *MNRAS*, 392, 590
 Bate, M. R. 2009b, *MNRAS*, 392, 1363
 Bate, M. R., & Bonnell, I. A. 2005, *MNRAS*, 356, 1201
 Bate, M. R., Bonnell, I. A., & Bromm, V. 2003, *MNRAS*, 339, 577
 Bleuler, A., & Teyssier, R. 2014, *MNRAS*, 445, 4015
 Bonnell, I. A., & Rice, W. K. M. 2008, *Science*, 321, 1060
 Bonnell, I. A., Clarke, C. J., & Bate, M. R. 2006, *MNRAS*, 368, 1296
 Bonnell, I. A., Smith, R. J., Clark, P. C., & Bate, M. R. 2011, *MNRAS*, 410, 2339
 Chabrier, G. 2003, *PASP*, 115, 763
 Commerçon, B., Hennebelle, P., & Henning, T. 2011, *ApJ*, 742, L9
 Dib, S., Schmeja, S., & Hony, S. 2017, *MNRAS*, 464, 1738
 Elmegreen, B. G., Klessen, R. S., & Wilson, C. D. 2008, *ApJ*, 681, 365
 Espinosa Lara, F., & Rieutord, M. 2013, *A&A*, 552, A35
 Federrath, C., Klessen, R. S., & Schmidt, W. 2008, *ApJ*, 688, L79
 Federrath, C., Banerjee, R., Clark, P. C., & Klessen, R. S. 2010, *ApJ*, 713, 269
 Fromang, S., Hennebelle, P., & Teyssier, R. 2006, *A&A*, 457, 371
 Girichidis, P., Federrath, C., Banerjee, R., & Klessen, R. S. 2011, *MNRAS*, 413, 2741
 Gong, M., & Ostriker, E. C. 2015, *ApJ*, 806, 31
 Guszejnov, D., Krumholz, M. R., & Hopkins, P. F. 2016, *MNRAS*, 458, 673
 Hennebelle, P. 2012, *A&A*, 545, A147
 Hennebelle, P. 2018, *A&A*, 611, A24
 Hennebelle, P., & Chabrier, G. 2008, *ApJ*, 684, 395
 Hennebelle, P., & Chabrier, G. 2009, *ApJ*, 702, 1428
 Hennebelle, P., & Chabrier, G. 2013, *ApJ*, 770, 150
 Hennebelle, P., & Falgarone, E. 2012, *A&A Rev.*, 20, 55
 Hennebelle, P., Commerçon, B., Joos, M., et al. 2011, *A&A*, 528, A72
 Hopkins, P. F. 2012, *MNRAS*, 423, 2037
 Jappsen, A.-K., Klessen, R. S., Larson, R. B., Li, Y., & Mac Low, M.-M. 2005, *A&A*, 435, 611
 Jog, C. J. 2013, *MNRAS*, 434, L56
 Könyves, V., André, P., Men'shchikov, A., et al. 2015, *A&A*, 584, A91
 Kroupa, P. 2001, *MNRAS*, 322, 231
 Krumholz, M. R. 2011, *ApJ*, 743, 110
 Krumholz, M. R., McKee, C. F., & Klein, R. I. 2004, *ApJ*, 611, 399
 Krumholz, M. R., Klein, R. I., & McKee, C. F. 2007a, *ApJ*, 656, 959
 Krumholz, M. R., Stone, J. M., & Gardiner, T. A. 2007b, *ApJ*, 671, 518
 Larson, R. B. 1969, *MNRAS*, 145, 271
 Larson, R. B. 1985, *MNRAS*, 214, 379
 Lee, Y.-N., & Hennebelle, P. 2016a, *A&A*, 591, A30
 Lee, Y.-N., & Hennebelle, P. 2016b, *A&A*, 591, A31
 Lee, Y. N., & Hennebelle, P. 2018, *A&A*, 611, A88 (Paper I)
 Lee, Y.-N., Hennebelle, P., & Chabrier, G. 2017, *ApJ*, 847, 114
 Masunaga, H., Miyama, S. M., & Inutsuka, S.-i. 1998, *ApJ*, 495, 346
 Motte, F., André, P., & Neri, R. 1998, *A&A*, 336, 150
 Myers, A. T., McKee, C. F., Cunningham, A. J., Klein, R. I., & Krumholz, M. R. 2013, *ApJ*, 766, 97
 Ntormousi, E., & Hennebelle, P. 2015, *A&A*, 574, A130
 Offner, S. S. R., Clark, P. C., Hennebelle, P., et al. 2014, *Protostars and Planets VI*, 53
 Padoan, P., Nordlund, A., & Jones, B. J. T. 1997, *MNRAS*, 288, 145
 Peters, T., Banerjee, R., Klessen, R. S., & Mac Low, M.-M. 2011, *ApJ*, 729, 72
 Rees, M. J. 1976, *MNRAS*, 176, 483
 Renaud, F., Bournaud, F., Kraljic, K., & Duc, P.-A. 2014, *MNRAS*, 442, L33
 Rieutord, M., & Espinosa, L. F. 2013, in *SF2A-2013: Proceedings of the Annual meeting of the French Society of Astronomy and Astrophysics*, ed. L. Cambresy, F. Martins, E. Nuss, & A. Palacios, 101
 Shu, F. H. 1977, *ApJ*, 214, 488
 Teyssier, R. 2002, *A&A*, 385, 337
 Vaytet, N., & Haugbølle, T. 2017, *A&A*, 598, A116
 Vaytet, N., Audit, E., Chabrier, G., Commerçon, B., & Masson, J. 2012, *A&A*, 543, A60
 Vázquez-Semadeni, E. 1994, *ApJ*, 423, 681
 Whitworth, A., Bate, M. R., Nordlund, Å., Reipurth, B., & Zinnecker, H. 2007, *Protostars and Planets V*, 459

Appendix A: Sink accretion scheme

The thresholding scheme for sink accretion by [Bleuler & Teyssier \(2014\)](#) was used in this study. Within the sink accretion radius, four times the smallest cell size, a fraction c_{acc} of the mass exceeding the density threshold n_{sink} is accreted onto the sink, and by default, $c_{\text{acc}} = 0.75$. When the mass from a cell is accreted by multiple sinks, the algorithm treats the sinks in decreasing order in terms of mass to ensure that more massive sinks accrete more mass. We performed a simulation with all parameters identical to C10h, except that $c_{\text{acc}} = 0.1$. As shown in [Fig. A.1](#), the stellar mass distribution does not differ significantly from that of run C10h ([Fig. 2](#)), ensuring that the accretion scheme does not have a strong effect on the final mass of the stars.

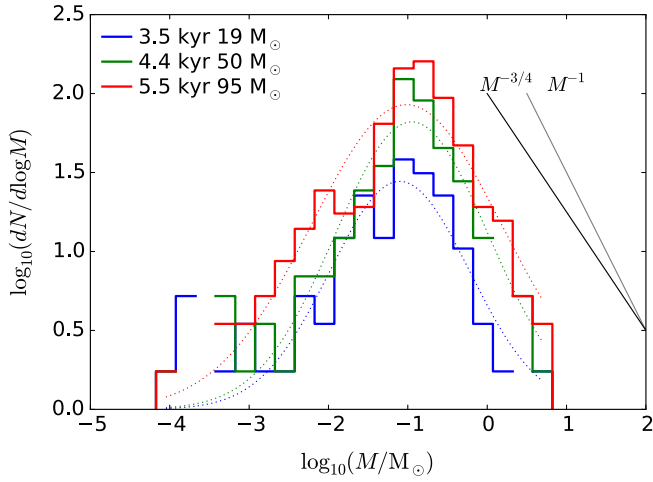


Fig. A.1. Stellar distributions of runs with a smoothed two-slope polytropic eos with $\gamma = 5/3$, $n_{\text{ad}} = 10^{10} \text{ cm}^{-3}$, and $c_{\text{acc}} = 0.1$ instead of 0.75 as in all the other runs. The peak of the distribution is not varied compared to run C10h.

Appendix B: Perturbation mass

The mass of the perturbation is equal to

$$\begin{aligned}
 M_p(r_p, \delta r_p, \eta) &= \frac{Ac_s^2}{G} \int_{\delta r=0}^{\delta r_p} \int_{\theta=-0}^{\pi} \left(\frac{1}{r_e^2} + \frac{\eta}{r_p^2} \right) \sin \theta d\theta \delta r^2 d\delta r \\
 &= \frac{Ac_s^2}{G} \int_{\delta r=0}^{\delta r_p} \int_{\cos \theta=-1}^1 \left(\frac{1}{r_e^2} + \frac{\eta}{r_p^2} \right) d \cos \theta \delta r^2 d\delta r \\
 &= \frac{Ac_s^2}{G} \int_{\delta r=0}^{\delta r_p} \left[-\frac{\log r_e}{r_p \delta r} + \frac{\eta \cos \theta}{r_p^2} \right]_{\cos \theta=-1}^1 \delta r^2 d\delta r \\
 &= \frac{Ac_s^2}{G} r_p \int_{u=0}^{u_p} \left[\log \left(\frac{1+u}{1-u} \right) u + 2\eta u^2 \right] du \\
 &= \frac{Ac_s^2}{G} r_p \left[u_p - \frac{1-u_p^2}{2} \log \left(\frac{1+u_p}{1-u_p} \right) + \frac{2}{3} \eta u_p^3 \right] \\
 &= \frac{Ac_s^2}{G} r_p m_p(u_p, \eta), \tag{B.1}
 \end{aligned}$$

where the normalized quantities $u = \delta r/r_p$ and $u_p = \delta r_p/r_p$.

Appendix C: Tidal forces in the simulations

In the vicinity of an accreting point mass, two contributions have to be considered. First the r^{-2} gravitational force induced by the central object, and second the r^{-1} force associated with the r^{-2} density profile envelope. Both have a positive eigenvalue, λ_3 , and two negative ones, $\lambda_1 = \lambda_2$. It can be shown that for the r^{-2} gravitational field, $\lambda_3/\lambda_1 = -2$ while for the second one $\lambda_3/\lambda_1 = -1$.

In order to assess the importance of tidal forces in our simulations, we calculated the gravitational stress tensor. We first averaged λ_3 and λ_1 in density bins, and then plotted the absolute value of their ratio. [Figure C.1](#) shows the result from run C10h at 6.1 and 9.3 kyr. Low densities correspond to the outer region of the cloud that is dominated by the tidal field of the global density distribution of the cloud and by the central cluster. At high densities ($> n_{\text{sink}} = 10^{10} \text{ cm}^{-3}$), corresponding to regions in the vicinity of sink particles, the destructive tidal force is strong, such that no core formation is allowed nearby. This illustrates the dominating effect of the gravitational field generated by the sink particle.

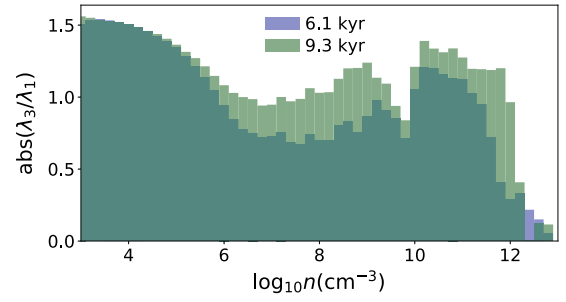


Fig. C.1. Tidal forces in run C10h. The absolute value of the ratio between the highest and lowest eigenvalues of the gravitational stress tensor λ_3/λ_1 is plotted against local density at 6.1 and 9.3 kyr. At very low density, corresponding to the outer region of the cloud, the gravitational field is dominated by the global density distribution of the cloud and by the central cluster, and thus $-2 < \lambda_3/\lambda_1 < -1$. The tidal forces become less destructive at slightly higher densities. At extremely high density ($> n_{\text{sink}} = 10^{10} \text{ cm}^{-3}$), corresponding to regions in the vicinity of existing sinks, the tidal forces become locally very destructive and prevent nearby sink formation.

Appendix D: 1D calculation of the gravitational energy

The expression of the 1D gravitational energy is

$$\begin{aligned}
 &\int_{-\delta r_p}^{\delta r_p} \rho(\delta r) g(\delta r) \delta r d\delta r \\
 &= \frac{(Ac_s^2)^2}{2\pi G r_p} \left\{ -\frac{GM_L}{Ac_s^2 r_p} \left[\frac{-8u_p^3}{3(1-u_p^2)^3} - \frac{2(\eta-1)u_p}{1-u_p^2} \right. \right. \\
 &\quad \left. \left. + (\eta-1) \log \left(\frac{1+u_p}{1-u_p} \right) \right] \right. \\
 &\quad \left. + \frac{4u_p^3}{(1-u_p^2)^2} - \frac{16}{3} \eta u_p - \frac{4u_p}{1-u_p^2} - \frac{4\eta}{3} \frac{u_p}{1-u_p^2} - \frac{4}{9} \eta^2 u_p^3 \right. \\
 &\quad \left. + 2 \log \left(\frac{1+u_p}{1-u_p} \right) + \frac{10}{3} \eta \log \left(\frac{1+u_p}{1-u_p} \right) \right\} \\
 &= \frac{(Ac_s^2)^2}{2\pi G r_p} \mathcal{E}_{1D,g}(r_p, u_p, \eta). \tag{D.1}
 \end{aligned}$$

Appendix E: 3D calculation of gravitational energy

We define ξ the angle between \mathbf{r}_e and $\delta\mathbf{r}$, and θ the angle between $\delta\mathbf{r}$ and $-\mathbf{r}_p$. Projected onto the direction of $\delta\mathbf{r}$, the gravitational fields have the values

$$g_L(\mathbf{r}_e) = g_{L,a}(\mathbf{r}_e) - g_{L,c}(\mathbf{r}_e) = -\frac{GM_L}{r_e^2} \cos \xi - \frac{GM_L}{r_p^2} \cos \theta, \quad (\text{E.1})$$

$$g_e(\mathbf{r}_e) = g_{e,a}(\mathbf{r}_e) - g_{e,c}(\mathbf{r}_e) = -\frac{2Ac_s^2}{r_e} \cos \xi - \frac{2Ac_s^2}{r_p} \cos \theta, \quad (\text{E.2})$$

$$g_p(\mathbf{r}_e) = -\eta \frac{2Ac_s^2}{3r_p^2} \delta\mathbf{r}, \quad (\text{E.3})$$

where the subscripts a and c signify the value at the point considered and the value at the center of the perturbation. The local density is

$$\rho(\mathbf{r}_e) = \frac{Ac_s^2}{2\pi G} \left(\frac{1}{r_e^2} + \frac{\eta}{r_p^2} \right). \quad (\text{E.4})$$

We have the trigonometric relations

$$r_e^2 = r_p^2 + \delta r^2 - 2r_p \delta r \cos \theta \quad \text{and} \quad (\text{E.5})$$

$$r_p^2 = r_e^2 + \delta r^2 - 2r_e \delta r \cos \xi, \quad (\text{E.6})$$

and we deduce $\cos \xi / r_e = [1 + (\delta r^2 - r_p^2) / r_e^2] / (2\delta r)$. The contribution to the gravity at the center of the perturbation from the central star and from the envelop behave in the same way, and the normalized integration gives

$$\begin{aligned} \mathcal{E}_{3D,L,c} &= \mathcal{E}_{3D,e,c} \\ &= \int_{\delta r=0}^{\delta r_p} \int_{\theta=0}^{\pi} -\frac{\cos \theta}{r_p^2} \left(\frac{1}{r_e^2} + \frac{\eta}{r_p^2} \right) \delta r^3 \sin \theta d\theta d\delta r \\ &= \frac{u_p(3-u_p^2)}{4} + \frac{u_p^4 + 2u_p^2 - 3}{8} \log \left(\frac{1+u_p}{1-u_p} \right). \end{aligned} \quad (\text{E.7})$$

Considering the integration of Eq. (12) separately for each gravitation term without subtracting the mean gravity field, we obtain

$$\begin{aligned} \mathcal{E}_{3D,L,a} &= \frac{1}{M_L Ac_s^2} \int_{V_p} \rho \mathbf{g}_{L,a} \cdot \delta \mathbf{r} dV \\ &= - \int_{\delta r=0}^{\delta r_p} \int_{\theta=0}^{\pi} \frac{\cos \xi}{r_e^2} \left(\frac{1}{r_e^2} + \frac{\eta}{r_p^2} \right) \sin \theta d\theta \delta r^3 d\delta r \\ &= - \int_{\delta r=0}^{\delta r_p} \int_{\cos \theta=-1}^1 \frac{\delta r^2}{2} \left(\frac{1}{r_e^3} + \frac{\eta}{r_e r_p^2} \right) \\ &\quad \times \left(1 + \frac{\delta r^2 - r_p^2}{r_e^2} \right) d \cos \theta d\delta r \\ &= - \int_{\delta r=0}^{\delta r_p} \frac{\delta r}{2r_p} \left[\frac{1}{r_e} - \frac{\eta r_e}{r_p^2} - (r_p^2 - \delta r^2) \right. \\ &\quad \left. \times \left(\frac{1}{3r_e^2} + \frac{\eta}{r_e r_p^2} \right) \right] \Big|_{\cos \theta=-1}^1 d\delta r \end{aligned} \quad (\text{E.8})$$

$$\begin{aligned} &= - \int_{u=0}^{u_p} \left(\frac{u}{1-u^2} - \frac{(3+u^2)u}{3(1-u^2)^2} \right) u du \\ &= - \left[-\frac{4}{3} u_p + \log \left(\frac{1+u_p}{1-u_p} \right) - \frac{2}{3} \frac{u_p}{1-u_p^2} \right], \quad \text{and thus} \end{aligned}$$

$$\mathcal{E}_{3D,L} = \mathcal{E}_{3D,L,a} + \mathcal{E}_{3D,L,c}, \quad (\text{E.9})$$

$$\begin{aligned} \mathcal{E}_{3D,e,a} &= \frac{G}{(Ac_s^2)^2 r_p} \int_{V_p} \rho \mathbf{g}_{e,a} \cdot \delta \mathbf{r} dV \\ &= -\frac{1}{r_p} \int_{\delta r=0}^{\delta r_p} \int_{\theta=0}^{\pi} \frac{2 \cos \xi}{r_e} \left(\frac{1}{r_e^2} + \frac{\eta}{r_p^2} \right) \sin \theta d\theta \delta r^3 d\delta r \\ &= -\frac{1}{r_p} \int_{\delta r=0}^{\delta r_p} \int_{\cos \theta=-1}^1 \left(\frac{1}{r_e^2} + \frac{\eta}{r_p^2} \right) \left(1 + \frac{\delta r^2 - r_p^2}{r_e^2} \right) d \cos \theta \delta r^2 d\delta r \\ &= \int_{\delta r=0}^{\delta r_p} \frac{\delta r^2}{r_p} \left[\frac{\log r_e}{r_p \delta r} - \frac{\eta \cos \theta}{r_p^2} + \frac{r_p^2 - \delta r^2}{r_p \delta r} \right. \\ &\quad \left. \times \left(\frac{1}{2r_e^2} - \frac{\eta \log r_e}{r_p^2} \right) \right] \Big|_{\cos \theta=-1}^1 d\delta r \\ &= \int_{u=0}^{u_p} \left\{ -u \log \left(\frac{1+u}{1-u} \right) + \frac{2u^2}{1-u^2} \right. \\ &\quad \left. + \eta \left[u(1-u^2) \log \left(\frac{1+u}{1-u} \right) - 2u^2 \right] \right\} du \\ &= \left\{ \frac{3-u_p^2}{2} \log \left(\frac{1+u_p}{1-u_p} \right) - 3u_p \right. \\ &\quad \left. + \eta \left[\frac{u_p}{2} - \frac{5u_p^3}{6} - \left(\frac{1-u_p^2}{2} \right)^2 \log \left(\frac{1+u_p}{1-u_p} \right) \right] \right\}, \end{aligned} \quad (\text{E.10})$$

leading to

$$\mathcal{E}_{3D,e} = \mathcal{E}_{3D,e,a} + \mathcal{E}_{3D,e,c}, \quad (\text{E.11})$$

$$\begin{aligned} \mathcal{E}_{3D,p} &= \frac{G}{(Ac_s^2)^2 r_p} \int_{V_p} \rho \mathbf{g}_p \cdot \delta \mathbf{r} dV \\ &= -\eta \frac{2}{3} \frac{1}{r_p^3} \int_{\delta r=0}^{\delta r_p} \int_{\theta=0}^{\pi} \left(\frac{1}{r_e^2} + \frac{\eta}{r_p^2} \right) \sin \theta d\theta \delta r^4 d\delta r \\ &= -\eta \frac{2}{3} \frac{1}{r_p^3} \int_{\delta r=0}^{\delta r_p} \int_{\cos \theta=-1}^1 \left(\frac{1}{r_e^2} + \frac{\eta}{r_p^2} \right) d \cos \theta \delta r^4 d\delta r \\ &= -\eta \frac{2}{3} \frac{1}{r_p^3} \int_{\delta r=0}^{\delta r_p} \left[-\frac{\log r_e}{r_p \delta r} + \frac{\eta \cos \theta}{r_p^2} \right] \Big|_{\cos \theta=-1}^1 \delta r^4 d\delta r \end{aligned}$$

$$\begin{aligned}
 &= -\eta \frac{2}{3} \int_{u=0}^{u_p} \left[u^3 \log\left(\frac{1+u}{1-u}\right) + 2\eta u^4 \right] du \\
 &= -\eta \frac{2}{3} \left[\frac{u_p}{2} + \frac{u_p^3}{6} + \eta \frac{2u_p^5}{5} - \frac{1-u_p^4}{4} \log\left(\frac{1+u_p}{1-u_p}\right) \right], \quad (\text{E.12})
 \end{aligned}$$

where $u = \delta r/r_p$, and $u_p = \delta r_p/r_p$. The condition for a second core forming near the initial central core is that $E_g(r_p, \delta r_p) \leq 0$ and that $M(r_p, \delta r_p, \eta) = M_L$. Substituting Eqs. (E.9), (E.11), and (E.12) and (17) into Eq. (12) reduces the latter to Eq. (25).

Appendix F: Density fluctuations: model II

Since the density fluctuations are important and they control the fragmentation around the accreting objects, we explored a second model (model II) to determine the robustness of our conclusions. We assumed that the turbulence follows a Larson relation inside the cloud and is conserved during collapse (this assumption may not be accurate as the collapse likely generates turbulent fluctuations), we have

$$\mathcal{M}(\tilde{r}_p) = \frac{v_t(\tilde{r}_p)}{c_s} = \frac{v_{t,\text{cloud}}}{c_s} \left(\frac{r_0(r_p)}{r_{\text{cloud}}} \right)^{\frac{1}{6}} = \mathcal{M}_{\text{cloud}} \left(\frac{M(r_p)}{M_{\text{cloud}}} \right)^{\frac{1}{6}}, \quad (\text{F.1})$$

where v_t , r_0 , $v_{t,\text{cloud}}$, r_{cloud} , and $\mathcal{M}_{\text{cloud}}$ are the turbulent velocity at r_p , the radius that corresponds to the mass enclosed inside radius r_p before the local mass concentration (at cloud average density), the turbulent velocity at cloud scale, the radius of the cloud, and the Mach number of the cloud. The mass $M(r_p)$ contained inside r_p takes the envelope and the central mass into account and can be expressed with the normalized form $M(r_p) = M_L(\tilde{r}_p + 1)$. This leads to

$$\mathcal{M}(\tilde{r}_p) = \mathcal{M}_{\text{cloud}} \left(\frac{M_L}{M_{\text{cloud}}} \right)^{\frac{1}{6}} (1 + \tilde{r}_p)^{\frac{1}{6}} = \mathcal{M}_0 (1 + \tilde{r}_p)^{\frac{1}{6}}. \quad (\text{F.2})$$

The local lognormal dispersion is therefore

$$\sigma^2(\tilde{r}_p) = \log\left(1 + b^2 \mathcal{M}_0^2 (1 + \tilde{r}_p)^{\frac{1}{3}}\right). \quad (\text{F.3})$$

The initial Mach number of our canonical run is ~ 20 , and $M_L/M_{\text{cloud}} \sim 10^{-2}/10^3 = 10^{-5}$. These values typically yield $\mathcal{M}_0 = \mathcal{M}_{\text{cloud}}(M_L/M_{\text{cloud}})^{1/6} \sim 2-3$. An important difference between the two assumptions made in models I and II is that the second estimate depends on the initial conditions, while the first is entirely local.

We performed numerical integrations for several values of \mathcal{M}_0 . Figure F.1 shows the resulting $\mathcal{N}(\tilde{r}_p)$, without considering the thermal support. We defined the critical radius \tilde{r}_p^* at which one self-gravitating mass M_L is expected, as marked with circles in the figure (model I is also shown for comparison).

The resulting $M_F = (1 + \tilde{r}_p^*)M_L$ is displayed in Fig. F.2 and should be compared to Fig. 11. When we also consider the thermal energy of the perturbation, the protected radius is increased since more support is present. In Fig. F.2 we also show results with thermal support using $A = 2, 5, 10$, and 20 . The effect of thermal support is more prominent when A is small, imposing a lower limit on \mathcal{M}_0 below which a star prevents its surrounding gas from fragmenting and will grow to become massive. The

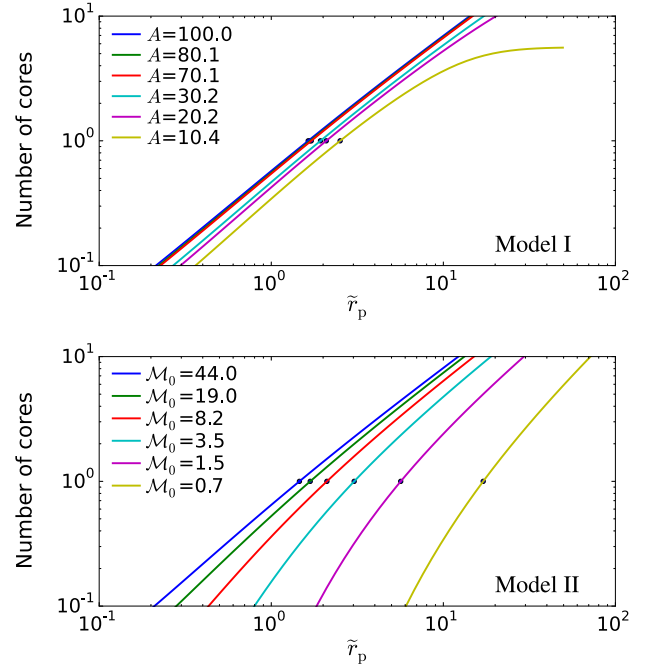


Fig. F.1. Probable number of self-gravitating cores found within radius \tilde{r}_p . *Upper panel:* Model I plotted with $\epsilon = 1$ and for several values of the density envelope amplitude, A . *Lower panel:* Model II without thermal support for several values of the global cloud Mach number, \mathcal{M}_0 . The circles mark the values where one self-gravitating core is found. In the range of our interest, that is, where $\mathcal{N}(\tilde{r}_p)$ equals a few, there is an almost linear dependance between $\mathcal{N}(\tilde{r}_p)$ and \tilde{r}_p .

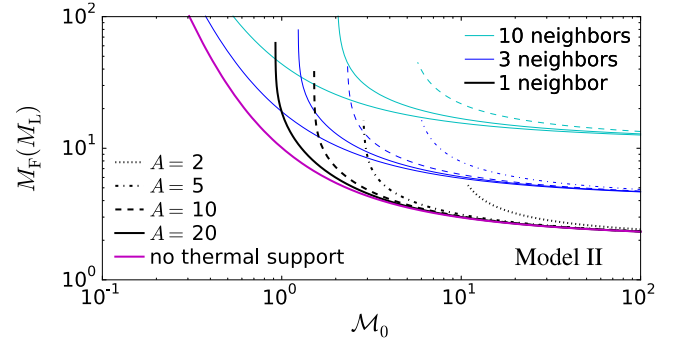


Fig. F.2. Final mass M_F in units of M_L for model II. M_F is plotted against the level of turbulence for cases with $A = 2, 5, 10$, and 20 , and without thermal support ($A \rightarrow \infty$, magenta). Model II also shows that M_F is expected to be larger than 3 when the envelope is truncated at $\mathcal{N}(\tilde{r}_p) = 1$, and > 5 when $\mathcal{N}(\tilde{r}_p) = 3$ (blue thin lines).

physical interpretation is that when the envelope density is low, stronger fluctuations are needed to create multiple stars, otherwise one star will dominate and prevent any further formation once it is formed. This is in good agreement with the result of Girichidis et al. (2011), who reported that clumps with an r^{-2} profile and weak turbulence do not fragment. For $A \sim 10$, as measured in Paper I (left panels of Fig. 4), the condition $\mathcal{N} = 1$ gives at least $M_F \sim 10M_L$ for any \mathcal{M}_0 lower than ~ 2 . Figure 8 shows that this is in good agreement with the value inferred from the simulations in the sense that the model predicts that the accreting envelope, protected from gravitational fragmentation, is several times the mass of the first Larson core.